Chem Soc Rev

REVIEW ARTICLE

View Article Online
View Journal | View Issue



Cite this: *Chem. Soc. Rev.*, 2014, 43, 7067

# Heteroatom-doped graphene materials: syntheses, properties and applications

Xuewan Wang,[a] Gengzhi Sun,[a] Parimal Routh,[a] Dong-Hwan Kim,[a] Wei Huang[b] and Peng Chen*[a]

Received 29th April 2014

DOI: 10.1039/c4cs00141a

www.rsc.org/csr

Heteroatom doping can endow graphene with various new or improved electromagnetic, physicochemical, optical, and structural properties. This greatly extends the arsenal of graphene materials and their potential for a spectrum of applications. Considering the latest developments, we comprehensively and critically discuss the syntheses, properties and emerging applications of the growing family of heteroatom-doped graphene materials. The advantages, disadvantages, and preferential doping features of current synthesis approaches are compared, aiming to provide clues for developing new and controllable synthetic routes. We emphasize the distinct properties resulting from various dopants, different doping levels and configurations, and synergistic effects from co-dopants, hoping to assist a better understanding of doped graphene materials. The mechanisms underlying their advantageous uses for energy storage, energy conversion, sensing, and gas storage are highlighted, aiming to stimulate more competent applications.

## 1 Introduction

In the past decade, we have witnessed immense progress in graphene research since the first isolation of this "wonder material". Graphene has been changing the landscape of many fields in science and technology, particularly condensed matter physics,[1,2] electronics,[3,4] energy storage and conversion,[5–7] and biomedical research.[8–10] Tremendous efforts are still ongoing to uncover the full potential of graphene and its derivatives.

The fascinating properties of pristine graphene (single-atom-thick layer of $sp^2$ bonded carbon atoms tightly packed into a 2D honeycomb lattice) are now largely understood and well-recognized through extensive research in the past years.[11–13] Although the lack of intrinsic bandgap and catalytic abilities seems to greatly limit the practical applications of pristine graphene, the legend of this 2D material is going to continue owing to its structural transformability and highly tunable properties. As recently demonstrated, new properties and application opportunities arise when graphene transforms from its native 2D structure to 0D (graphene quantum dots),[14–17] 1D (graphene nanoribbons)[18,19] or 3D (graphene foam) structures.[20–22]

[a] School of Chemical and Biomedical Engineering, Nanyang Technological University, 70 Nanyang Drive, 637457, Singapore. E-mail: ChenPeng@ntu.edu.sg
[b] Singapore-Jiangsu Joint Research Center for Organic/Bio-Electronics and Information Displays & Institute of Advanced Materials (IAM), Nanjing Tech University, 30 South Puzhu Road, Nanjing, 211816, China

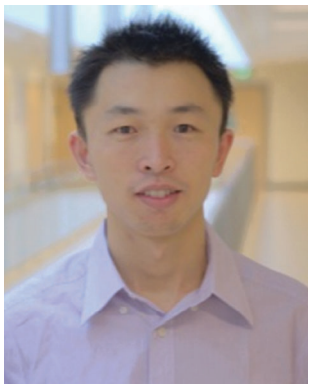

**Xuewan Wang**

*Xuewan Wang received his BS from Yantai University (China) in 2008 and MS from Zhejiang University (China) in 2011. He is currently a 3rd year PhD student in Prof. Peng Chen's group in Nanyang Technological University (Singapore). His main research focus is on the synthesis of graphene materials and their applications for energy storage and conversion, and sensing.*

**Peng Chen**

*Peng Chen is currently an Associate Professor in the School of Chemical and Biomedical Engineering at Nanyang Technological University (Singapore). He completed his PhD in the University of Missouri (Columbia) in 2002, followed by a period of postdoctoral research at Harvard University. His current research focuses on nanomaterials (particularly graphene), biosensors, and bionanotechnology, which has resulted in >120 publications.*

In addition, the physicochemical and electronic properties of graphene can be drastically altered by molecular and atomic doping.

Tailoring graphene properties by interacting molecules, which either donate or withdraw free electrons, has been demonstrated in many studies and discussed in recent review articles.[23–25] Herein, we focus the discussion on the doping of graphene with various heteroatoms (oxygen, boron, nitrogen, phosphor, sulfur, *etc.*), *i.e.*, the graphitic carbon atoms are substituted or covalently bonded by foreign atoms. Although several review articles focusing on specific dopants or particular applications have been published,[26–29] a more comprehensive and comparative review on this important and quickly evolving topic is necessary. In this article, the synthesis methods, properties and applications of graphene materials doped with various heteroatoms are reviewed extensively. We aim to cover the latest developments, underscore physical mechanisms, highlight unique application-specific advantages conferred by doping, and provide insightful comparison between doped and pristine graphene, different synthesis routes, different dopant atoms, and different doping configurations.

# 2 Synthesis methods

A large variety of methods have already been developed for the synthesis of graphene materials, from which various doping strategies could be derived. The current methods for heteroatom doping can be categorized into *in situ* approaches and post-treatment approaches. *In situ* approaches, which simultaneously achieve graphene synthesis and heteroatom doping, include chemical vapor deposition (CVD), ball milling, and bottom-up synthesis. Post-treatment methods include wet chemical methods, thermal annealing of graphene oxides (GO) with heteroatom precursors, plasma and arc-discharge approaches. In this section, these methods are discussed and compared in detail (Table 1).

## 2.1 *In situ* doping

**2.1.1 Chemical vapor deposition (CVD).** Many CVD methods have been developed to synthesize large, continuous, defect-free, single- or few-layered graphene films. The catalytic growth mechanism makes it a convenient route to dope heteroatoms during the formation of graphene films, particularly to incorporate heteroatoms directly into the graphitic carbon lattices.

Table 1 Summary of graphene doping techniques

| Methods | Precursors | Doping | Advantages and limitations | Ref. |
|---|---|---|---|---|
| CVD | $H_3BO_3$ + polystyrene | 4.3 at% B | Simultaneous growth and doping of large graphene sheet; controllable doping; complex process and high operating temperature; sometimes hazardous precursors and waste gases are produced; high cost and low yield. | 31 |
| | Phenylboronic acid | 1.5 at% B | | 36 |
| | $CH_4$ + $H_3NBH_3$ | 10–90 at% BN | | 33 |
| | $CH_4$ + $NH_3$ | 8.9 at% N | | 42 |
| | Sulfur in hexane | $<$0.6 at% S | | 44 |
| | Iodine + camphor | 3.1 at% I | | 46 |
| | Pyrimidine + thiophene | $\leq$5.7 N, 2.0 S at% | | 45 |
| Ball milling | Pristine graphite (PG) + $N_2$ | 14.8 wt% N | Simple and scalable process; doping only at edges; difficult to control the doping process. | 49 |
| | PG + sulfur powder | 4.94 at% S | | 53 |
| | PG + $Cl_2$/$Br_2$ | 5.85 Cl/2.78 Br at% | | 51 |
| Bottom-up synthesis | $CCl_4$ + K + $BBr_3$ | 2.56 at% B | Scalable solution-based reaction under mild conditions; unavoidable high oxygen content. | 54 |
| | $Li_3N$ + $CCl_4$ | 4.5–16.4 at% N | | 55 |
| | Pentachloropyridine + K | 3.0 at% N | | 56 |
| Thermal annealing | GO + $BCl_3$ | 0.88 at% B | Wide choices of dopant precursors (gases, liquids, or solids); controllable doping; high temperature required, but helpful to recover $sp^2$ carbon network. | 59 |
| | GO + $NH_3$ | 8 at% N | | 63 |
| | GO + melamine/PANI/PPy | 2–18 at% N | | 70 and 71 |
| | GO + ionic liquid | 22.1 N/1.16 P at% | | 75 and 76 |
| | GO + $H_2S$ | 1.2–1.7 at% S | | 77 |
| | GO + DDS + DDSe | 0.19 S, 0.05 Se at% | | 80 |
| | Graphite oxide + $Cl_2$/$Br_2$ | 5.9 Cl/9.93 Br at% | | 84 |
| Wet chemical method | GO + hydrazine | 4.5 at% N | Amenable to low-cost, low-temperature, solution-based mass production; easily achieve doping and decoration (*e.g.*, with various nanoparticles) simultaneously; conveniently form 3D gel structure. | 86 |
| | GO + urea | 10.13 at% N | | 91 |
| | GO + $NH_4SCN$ | 18.4 N, 12.3 S at% | | 95 |
| | GO + HF/HI | 1.38 F/4.33 I wt% | | 96 |
| | PG + $Cl_2$/$Br_2$ | 21 Cl/ 4 Br at% | | 99 |
| Plasma | GO + $N_2$ | 2.51 at% N | Short reaction time and low power consumption; low yield. | 108 |
| | CVD graphene + $Cl_2$ | 45.3 at% Cl | | 112 |
| Photo-chemistry | CVD graphene + $Cl_2$, xenon lamp irradiation | 8 at% Cl | Short reaction time and low power consumption; low yield. | 113 |
| Arc-discharge | PG + $NH_3$ | 1 at% N | Mass-production; high voltage or current required; low doping level; mainly multilayer graphene. | 114 |
| | PG + B/$B_2H_6$ | 3.1 at% B | | 115 |
| | PG + graphite fluoride | 10 wt% F | | 116 |

 

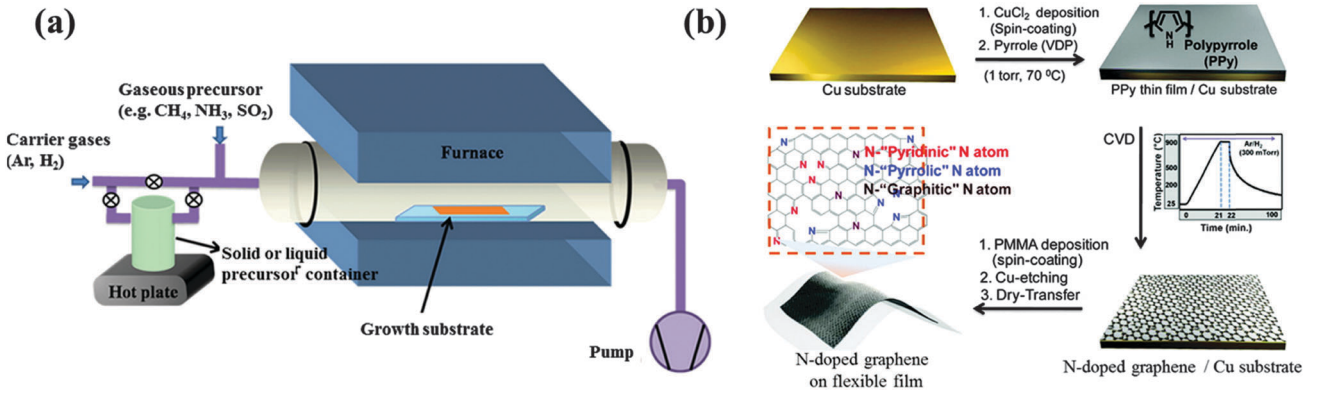


Fig. 1 (a) Experimental setup commonly used for CVD graphene doping. Adapted with permission from ref. 30. Copyright (2013) American Chemical Society. (b) N-doped graphene derived from polypyrrole. Adapted with permission from ref. 39. Copyright (2012) American Chemical Society.

As illustrated in Fig. 1a,[30] doping can occur by introducing solid, liquid, or gaseous precursors containing desired foreign atoms into the growth furnace together with the carbon sources. In some cases, carbon and foreign atom(s) share the same precursor. The co-doping of multiple species may also be achieved, aiming to create synergy between the co-dopants.

Because boron (B) and nitrogen (N) have similar sizes and valence electron numbers as carbon (C), it is relatively easier to incorporate them into graphene. For example, B-doped graphene with a doping level of 4.3 at% (atomic percentage) was grown on a copper (Cu) foil at 1000 °C under the protection of $H_2$/Ar atmosphere, using boric acid and polystyrene as the B and C sources, respectively.[31] These solid-phase feedstocks are sublimated upstream and transported by the carrier gases toward the growth substrate (Fig. 1a). B-doping was also realized using ethanol as the carbon source and boron powder as the B-precursor.[32] There are two bonding configurations of B atoms observed in CVD graphene lattice: "boron silane" boron ($BC_4$) and graphitic boron ($BC_3$). In contrast to the more commonly occurring $BC_3$ bonding (B replacing C in the hexagonal carbon lattice), $BC_4$ configuration is obtained due to the excess defects or edge sites. Dual B,N doped graphene was reported by Ajayan *et al*, using methane and ammonia borane ($NH_3$–$BH_3$) as the carbon and B,N sources, respectively.[33] The doping level can be tuned by adjusting the reaction parameters. At high doping levels, the resultant large-area B,N co-doped graphene contains B–N hybridized domains (with B/N ratio, ~1), as evidenced by the X-ray photoelectron spectroscopy (XPS) analyses. The incorporation of small BN domains (B/N ratio, 0.3–0.5) was also reported by Bepete *et al.*, employing boric acid powder and $N_2$ as the precursors.[34] Using nickel foam as the growth template, B, N, or (B,N)-doped 3D graphene was also reported, which, when compared with its 2D counterparts, offers a larger active surface area.[35]

In comparison with the use of multiprecursors, a single precursor, containing both C and alien atom is believed to be more convenient and controllable. For instance, homogeneous B-doping on a graphene monolayer was produced using phenylboronic acid as the sole precursor, without significantly compromising the transmittance and conductivity of the graphene film.[36] Pyridinic and pyrrolic N-doped graphene was synthesized using acetonitrile as the only precursor,[37] while pyridinic N-doped graphene was CVD-grown, using pyridine as the sole source.[38]

Heteroatom-containing polymers (sometimes embedded in the polymeric carrier matrix) can be directly vapor-deposited or spin-coated atop the metal catalyst for graphene growth and *in situ* doping. Such processes are safer without the use of high-temperature gases and can achieve patterned doping. In the work of Kwon *et al.*, pyrrole monomers vapored on a Cu substrate were polymerized by the presence of $Cu^{2+}$ ions, followed by CVD growth (Fig. 1b).[39] The obtained N-doped few-layered graphene contains 3.14 at% N with dominating pyrrolic N probably inherited from the polypyrrole precursor. Sun *et al.* directly spin-coated the mixture of N-rich melamine and PMMA on a Cu substrate for the growth of N-doped graphene at 1000 °C under atmospheric pressure, reaching a doping level of 2–3.5 at%.[40] It is known that melamine can evolve into two-dimensional graphene-like graphitic carbon nitride (g-$C_3N_4$).[41] Although the configuration of N-doping is mainly graphitic, the mobility of the obtained N-graphene is poor ($<10$ $cm^2$ $V^{-1}$ $s^{-1}$).[40]

A gaseous precursor is the most commonly used, for which the doping level can be readily controlled by the flow rates (and thus, the percentage ratio between the gaseous reactants). Further, Wei *et al.* firstly reported the experimental synthesis of N-doped graphene with $CH_4$ and $NH_3$ as the C and N sources, respectively.[42] The growth temperature and the ratio between $CH_4$ and $NH_3$ exert a considerable influence on the bonding structure of doped nitrogen. The few-layered N-graphene synthesized at 800 °C enjoys a high N level of 8.9 at%, among which graphitic N is the dominant species (as compared to the co-existing pyridinic and pyrrolic N),[42] whereas N-doped graphene synthesized at 1000 °C exhibits dominating pyridinic N and a small fraction of pyrrolic N.[43]

Fluorine gas ($F_2$) and F-containing compounds are toxic and too reactive at high temperatures. Therefore, to the best of our knowledge, there is still no report on the synthesis of F-doped graphene using the CVD method. Further, it is energetically unfavorable to incorporate large-sized atoms

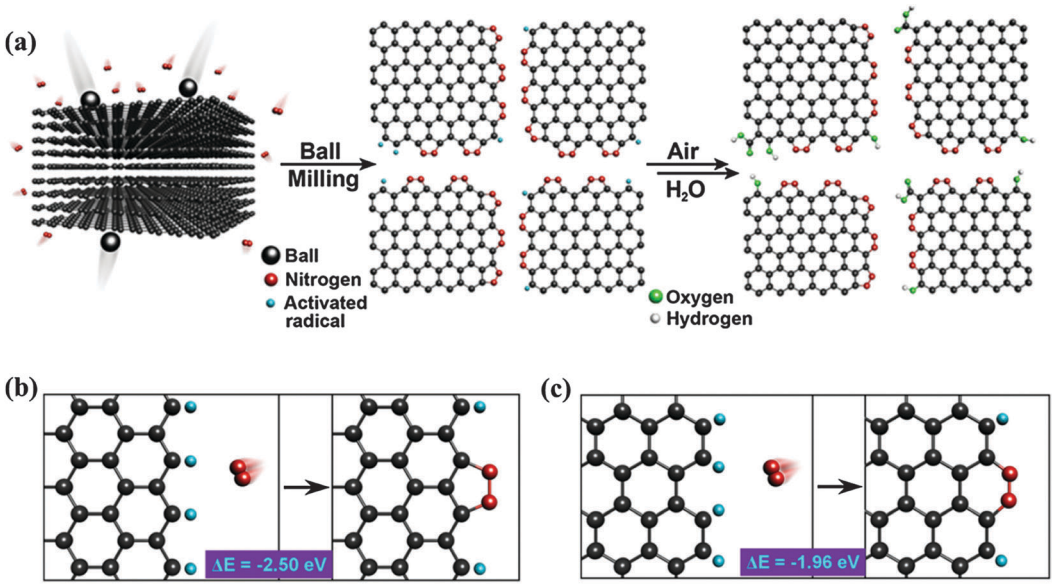


Fig. 2 (a) A schematic representation of the physical cracking of graphite flakes in a ball-mill crusher in the presence of nitrogen and subsequent exposure to air moisture to produce N-doped graphene nanoplates. (b and c) The formation of a 5-membered pyrazole ring/6-membered pyridazine ring after the reaction between the active zigzag-edge carbon atoms/armchair-edge carbon atoms and nitrogen. Adapted with permission from ref. 49. Copyright (2013) Nature Publishing Group.

(*e.g.*, silicon, Si; phosphorus, P; sulfur, S; chlorine, Cl; iodine, I) into graphene. Gao *et al.* demonstrated the CVD growth of S-doped graphene on a Cu substrate using sulfur powder dissolved in hexane as the precursor.[44] However, the S-doping level is extremely low (<0.6 at%), likely in the form of –C–S–C– and preferably at the defect sites due to the lowered binding energy. Xu *et al.* synthesized N, S co-doped graphene at a relatively low temperature of 700 °C using pyrimidine (N, C source) and thiophene (S, C source) as the precursors.[45] N and S atoms in the co-doped graphene are uniformly distributed with the doping levels of 3.7 to 5.7 at% and 0.7 to 2.0 at%, respectively. Apart from the –C–S–C– bonding configuration, –C–$SO_x$–C– is also speculated to exist. I-doped graphene was also made using the CVD method, where an iodine and camphor mixture was evaporated and pyrolyzed on a nickel substrate at 800 °C for 3 min.[46] All the I atoms (3.1 at%) are doped *via* ionic bonding in aggregated forms (*e.g.*, $I_3^-$ and $I_5^-$).

**2.1.2 Ball milling.** CVD approaches, however, involve high costs, which are only suitable for synthesizing thin-film graphene and not amenable to mass production. In comparison, ball milling is an effective way to massively produce graphene nanosheets at low cost by delaminating graphite and cracking the C–C bonds. It provides the unique possibility for graphene doping. The freshly formed active carbon species (*e.g.* carboradicals, carbocations and carbanions) at the edges can readily react with the dopants *via* mechanochemistry. Such an edge-selective functionalization process preserves the excellent crystallinity of the graphene basal plane (and thus, the electronic properties of graphene).[47,48]

By ball-milling graphite under $N_2$ atmosphere over 48 h, Jeon *et al.* successfully fixed uncleaved $N_2$ at the broken edges of graphene nanoplates with a high nitrogen content of 14.84 wt% (weight percentage) (Fig. 2a).[49] They proposed that aromatic 5-membered pyrazole and 6-membered pyridazine rings are energy-favorably formed at zigzag and armchair edges, respectively (Fig. 2b and c). It is more likely to form zigzag edges due to the larger density of states near the Fermi level than that of the armchair edges.[50] However, the stability of the 5N ring at the zigzag edges is inferior to the 6N ring at the armchair edges. In addition, the entropy gain from the grain size reduction and enthalpy increase from the edge functionalization facilitate the dispersion of graphene nanoplates in various polar solvents (*e.g.* water, methanol, isopropyl alcohol, DMF and NMP).[51,52] This is desirable for further solution-based processes.

Edge-sulfurized graphene nanoplatelets (SGnP) were also prepared by ball milling graphite in the presence of sulfur ($S_8$) with uniformly-distributed sulfur elements at a level of 4.94 at%.[53] Similarly, halogen atom-doped graphene nanoplates (ClGnP, BrGnP and IGnP) were synthesized in the presence of chlorine ($Cl_2$), bromine ($Br_2$) or iodine ($I_2$), respectively.[51] The decreasing doping levels (Cl at 5.89, Br at 2.78, and I at 0.95 at%) correlate with the decreasing chemical reactivity and increasing size of these elements. Analogous to ball milling, the N-doping of graphene was achieved by means of mechanically exfoliating graphene sheets by scotch-taping graphite in a nitrogen ambience.[50] The freshly generated edges were immediately passivated by nitrogen. Because doping and defects were absent in the basal plane, high mobility of 5000 $cm^2 V^{-1} s^{-1}$ was measured.

**2.1.3 Bottom-up synthesis.** Wurtz-type reductive coupling (WRC) reaction has been proposed as a bottom-up method for the preparation of high-quality heteroatom-doped graphene. By reacting tetrachloromethane ($CCl_4$) with potassium (K) in the presence of boron tribromide ($BBr_3$) under a mild condition (210 °C, for 10 min), B-doped few-layer graphene was

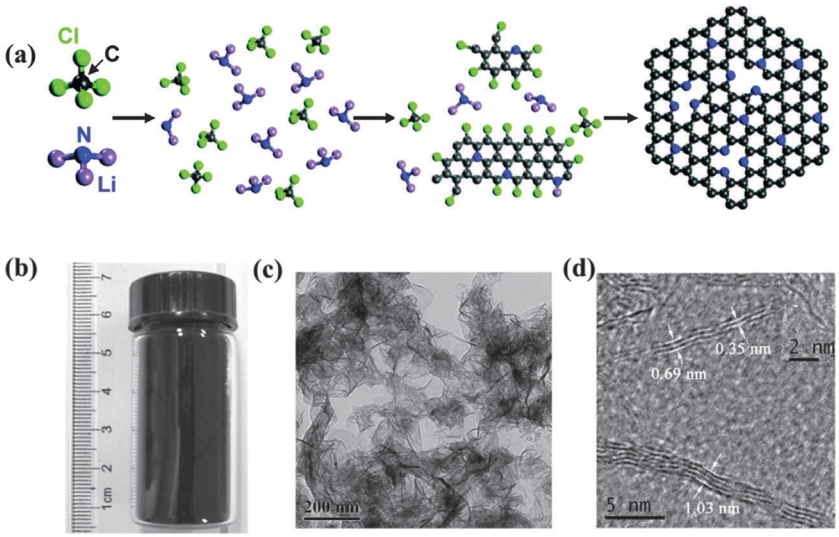


Fig. 3 (a) Proposed mechanism for the solvothermal synthesis of N-doped graphene *via* the reaction of $CCl_4$ and $Li_3N$, where the gray balls represent C atoms; blue, N; green, Cl; and purple, Li. (b) Vial containing the prepared N-doped graphene sample. (c and d) TEM images of the synthesized N-doped graphene samples. Adapted with permission from ref. 55. Copyright (2011) American Chemical Society.

successfully synthesized with a doping level of 2.56 at%, which could be tuned by adjusting the amount of B precursors.[54] Similarly, the gram-scale of N-doped graphene (4.5–16.4 at%) was synthesized from lithium nitride ($Li_3N$) and $CCl_4$ at 120 °C for 12 h or cyanuric chloride mixed with $Li_3N$ and $CCl_4$ at 350 °C for 6 h.[55] Graphitic N is prominent in the former reaction, while pyridinic and pyrrolic N are prevalent in the latter. Pyridinic N- and graphitic N-doped graphene was obtained by reacting pentachloropyridine with potassium at 160 °C.[56] Three reaction steps have been proposed for the formation of B/N-doped graphene (Fig. 3): (1) striping off halogens from halides; (2) the coupling and assembly of freshly formed –C≡C– and –C≡B/N– into two-dimensional hexagonal carbon clusters; and (3) the growth of B/N-doped graphene from these clusters.[54] Doping level can be readily controlled by the amount of heteroatom precursors for the WRC reaction. In comparison with CVD growth, it does not require transition metal catalysts, but high oxygen content will be unavoidably introduced.[57] Peng *et al.* developed a different strategy to synthesize N-doped graphene-like sheets by annealing the mixture of PANI and melamine with the addition of $Fe^{3+}$ ions at 900 °C.[58] Fe is believed to catalyze the formation of a sheet structure.

## 2.2 Post-synthesis treatment

**2.2.1 Thermal annealing.** Graphene oxides (GO) prepared by chemical exfoliation approaches can be regarded as O-doped graphene materials. The abundant oxygen functional groups and defects on GO can act as reactive sites for the doping of other heteroatoms. The thermal annealing of GO or reduced GO (rGO) at high temperatures is effective to recover the $sp^2$ carbon network and simultaneously achieve heteroatom doping with the presence of appropriate precursors. For instance, by annealing rGO in $BCl_3$ and Ar atmosphere at 800 °C for 2 h or in $NH_3$ and Ar atmosphere at 600 °C, B-doped (0.88 at%) or N-doped (3.06 at%) graphene was obtained.[59] Under such low annealing temperatures, only pyridinic and pyrrolic N are formed. Different from the samples prepared by CVD, B atoms are doped in the form of $BC_3$ and $BC_2O$, which may be due to the high oxygen content on rGO. A higher temperature is favorable for the formation of B–C bonding rather than B–O bonding.[60] N-doping is more commonly obtained by annealing GO under high-purity ammonia gas ($NH_3$), which is not only a nitrogen source but even a more effective reducing agent than $H_2$.[61]

It is unambiguous that temperature is a key factor to determine the N-doping efficiency and bonding configuration. Annealing GO in low-pressure $NH_3$/Ar atmosphere at different temperatures (from room temperature to 1100 °C), Li *et al.* found that N doping starts to occur at 300 °C and reaches the highest doping level of ~5 at% at 500 °C.[61] It is proposed that 500–600 °C is optimal for the overall stability of all the N species (amino, pyrrolic, pyridinic, and possibly graphitic N).[62] Using such temperatures, an even higher N-doping level of ~8 at% was reported.[63,64] At lower temperatures (300–500 °C), N bonding configurations include amino, amide, and pyrrolic N. The amino groups dominate as amino free radicals from ammonia react with the oxygenated groups on GO. In contrast, pyridinic and pyrrolic N are dominant at a temperature of >800 °C.[65–68] At a further elevated temperature, some pyridinic and pyrrolic N may be burnt by oxygen released from GO, leading to a decrease in the N content.[66] It was reported that annealing at 1100 °C for a long time promotes the formation of graphitic N in the carbon lattice.[67] These observations are consistent with the thermal stability of different N bonding configurations: graphitic N > pyridinic N > pyrrolic N. Moreover, Dai *et al.* demonstrated B,N co-doped graphene by simply thermally annealing GO in the presence of boric acid and $NH_3$ at 1000 °C.[69] They also suggested that the increase of annealing time facilitates the formation of BN clusters.

In addition to the annealing temperature, the doping efficiency and configuration also critically depend on the chosen

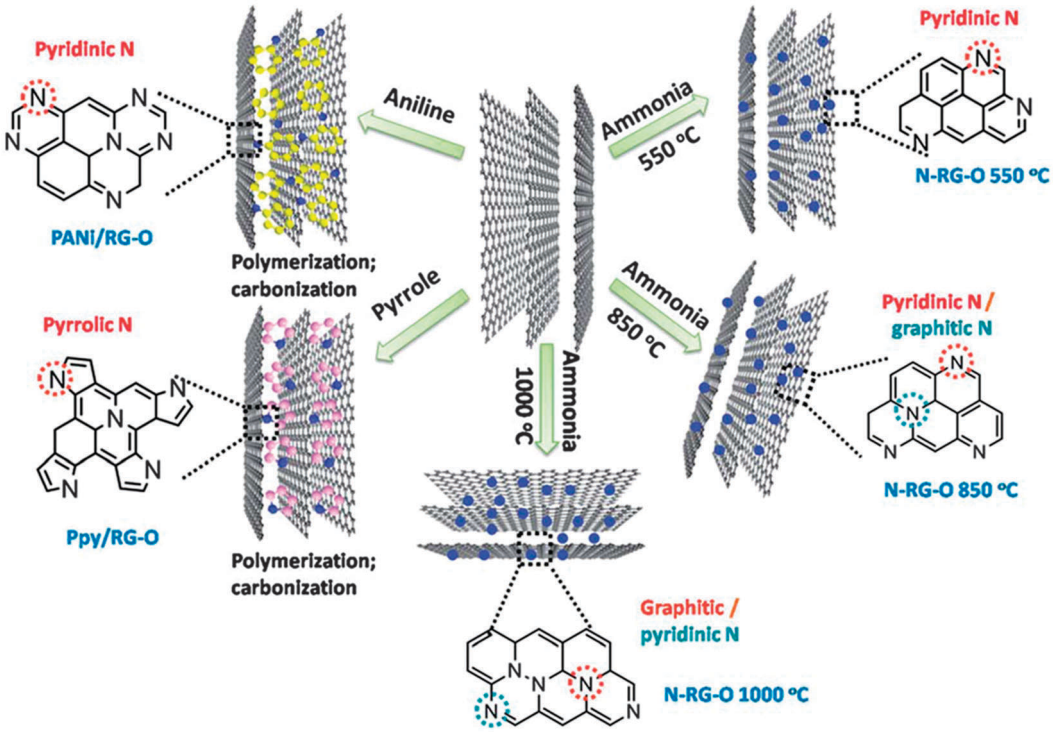


Fig. 4 N-doping configuration depends on the precursor and temperature. Adapted with permission from ref. 70. Copyright (2012) Royal Society of Chemistry.

precursor(s) (Fig. 4).[70] In addition to $NH_3$, melamine,[71] polyaniline (PANI),[70,72] polypyrrole (Ppy),[70] cyanamide[73] and dicyandiamide[74] have also been employed. Using these precursors, the N-doping level ranges from 2 to 18 at%. Ionic liquids (IL), which contain N and/or P and whose surface tension and surface energy match well with that of graphene, can serve as excellent doping sources. Liu *et al.* annealed IL-electrolyzed graphene at a really low temperature of 400 °C and obtained a high N/C ratio of 22.1%.[75] The N-bonding configuration is strongly dependent on the charge characteristics, viscosity, and other properties of the used ILs. For example, N-doped graphene synthesized using 1-butyl-3-methylimidazolium bromide ([Bmim]Br) shows the presence of pyrrolic N (major species) and graphitic N. In comparison, [Bmim][Ac] produced N-doped graphene shows dominant pyridinic N, while [Bmim]$PF_6$ produced N-doping is equally contributed by pyridinic and pyrrolic forms. Furthermore, using [Bmim]$PF_6$, but annealed at 1000 °C, P-doped graphene nanosheets (3–4 layers) were obtained.[76] P-doping (1.16 at%) equally exists in the two bonding configurations: P–C and P–O.

To avoid aggregation during the annealing process and ensure free gas transport, Yang *et al.* used porous silica to confine GO sheets for N- or S-doping (Fig. 5).[77] It was found that S-doping (1.2–1.7 at%) is less effective than N-doping, and S-doping occurring at the defect sites forms thiophene-like structure. The properties of GO (the abundance and composition of oxygenated groups) and chosen S-source ($H_2S$, $SO_2$ or $CS_2$) exert great influences on doping.[78] Seredych *et al.* doped S into graphene by heating rGO in $H_2S$ at 800 °C and 3 at% of S was introduced in the thiophenic groups and aromatic rings.[79] The XPS analyses indicate that neutral S, –SH, $–S_2–O–$ and –SO– co-existed in the resultant materials. The solid precursors normally used for S/Se doping include diphenyldisulfide (DDS),[80] phenyl disulfide (PDS),[81] benzyl disulfide (BDS),[82,83] and diphenyl diselenide (DDSe).[80,82] Using BDS and melamine as the precursors, N,S co-doped graphene was produced with 2.0 at% of S and 4.5 at% of N.[83]

For halogen doping, Poh *et al.* successfully synthesized Cl-, Br- and I-doped graphene (with the doping levels of 5.9, 9.93 and 2.31 at%, respectively) by the thermal exfoliation/reduction of graphite oxide in halogen gas atmosphere.[84] Considering the poor thermal stability of halogen-doped graphene, the doping process is conducted in a vacuum tight reactor with rapid temperature ramping/cooling rates. Similar to CVD processes, I-doping by this thermal process also relies on ionic bonding. The conductivity of Cl-graphene, Br-graphene and I-graphene increases in this order. On the other hand, their thermal stability decreases in the order in oxygen (but opposite in argon). Alternatively, Yao *et al.* prepared I-graphene by annealing GO and iodine in argon.[85] With the increase of temperature from 500 to 1100 °C, the content of I decreases from 1.21 to 0.83 wt%.

**2.2.2 Wet chemical methods.** We have discussed a number of doping strategies above. However, most of these methods require complex procedures and/or harsh conditions, low yield, or high cost. Therefore, efforts have been made to develop low-cost methods for the mass-production of doped graphene materials in the solution phase. Because of its amphiphilic property, GO can be well-dispersed in water and various solvents, and the oxygen functional groups on its surface

 

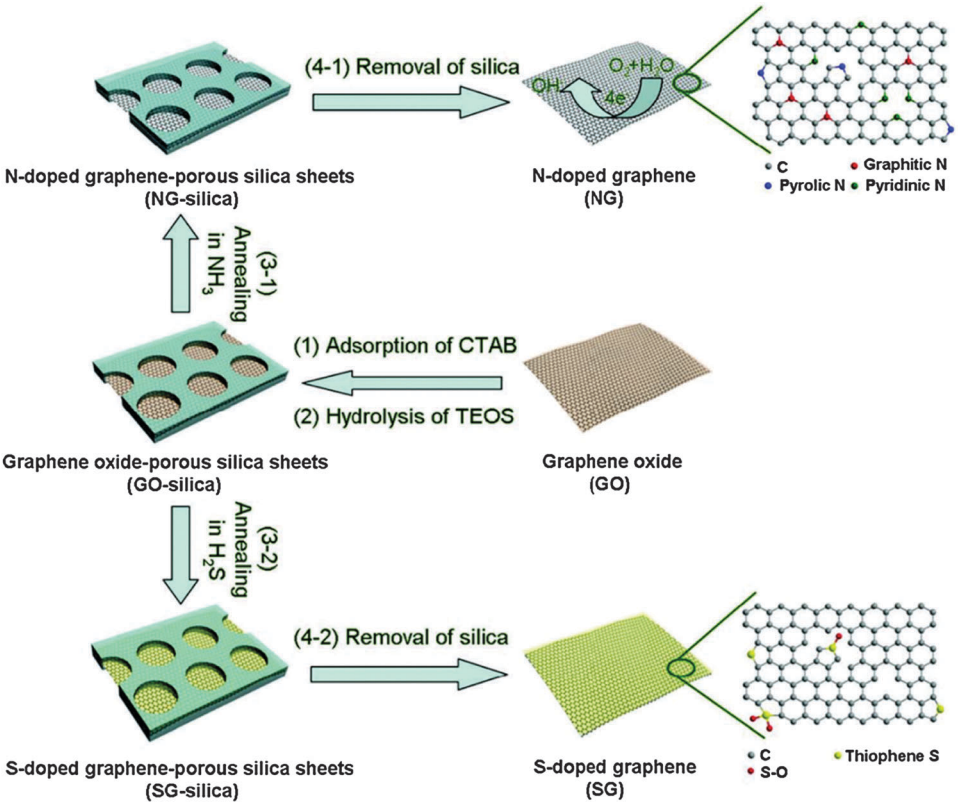


Fig. 5 N- or S-doping on porous silica confined GO sheets by thermal annealing. Adapted with permission from ref. 77. Copyright (2012) Wiley Publishing Group.

provide convenient chemical handles for reaction with heteroatom precursors. Hydrazine has been used for simultaneous GO reduction and N-doping in solution.[86,87] Ruoff's group reported that by hydrazine reduction, five member pyrazole rings with $N_2$ moiety form at the edges of a GO sheet.[88] Ammonia solution ($NH_4OH$) is another widely adopted N precursor due to its high reactivity at relatively low temperatures (*e.g.* 80 °C).[89,90] Urea,[91] hexamethylenetetramine,[92] dicyandiamide,[93] and hydroxylamine[94] can also serve as precursors for N doping because their decomposition leads to the gradual release of $NH_3$ during a hydrothermal process. The slow release of reactive $NH_3$ is desirable for high doping levels. Taking advantage of this, Sun *et al.* synthesized N-graphene (10.13 at% doping) using urea.[91] They proposed that $NH_3$ continually reacts with the oxygen functional groups of GO (*e.g.* –COOH, –OH) for the initial formation of amide and amine intermediates, which then instantaneously reorganize by dehydration and decarbonylation to form more stable pyridine- and pyrrole-like structures (Fig. 6a). Graphitic N can form by increasing the reaction time resulting from the cyclization rearrangement (Fig. 6b).

Su *et al.* used $NH_4SCN$, which decomposes into highly reactive species ($NH_3$, $H_2S$, $CS_2$) under hydrothermal condition, for N,S co-doping on GO.[95] The homogeneous doping of S (12.3 at%) and N (18.4 at%) is achieved. N exists in pyridinic (64%) and graphitic (36%) forms, while S mainly dopes at the defect sites and edges in the form of –C–$S_n$–C– ($n$ = 1 or 2, 55%), –C═S– (35%) and other moieties (*e.g.* –$SO_n$–, –SH). Garrido *et al.* modified GO with halogen atoms by hydrothermal approaches in HX solutions (X = F, Cl, Br or I), with doping levels of 4.38 (F), 2.28 (Cl), 5.36 (Br), and 4.33 (I) wt%.[96]

Halogen-doped graphene can also be obtained by the liquid-phase exfoliation (*e.g.*, sonication) of graphite halide.[97,98] However, the doping level cannot be tuned using such methods, and it is usually challenging to make a large amount of halogenated graphite except fluorinated graphite. Recently, Zheng *et al.* developed an interesting microwave-spark method to synthesize Cl- and Br-doped graphite in the presence of liquid chlorine and bromine, which could then be easily exfoliated into single-layered Cl-/Br-doped graphene sheets *via* sonication (Fig. 7).[99] Under the luminous microwave-sparks, active graphite flakes generated by a short temperature shock can react with halogen precursors. Subsequent rapid temperature decrease quenches the reaction and prevents the thermal decomposition of the resultant materials. The obtained graphene sheets contain high percentages of covalently bonded Cl and Br (21 at% and 4 at%, respectively). Different from GO, the resulting doped-graphene is strongly hydrophobic and disperses well in organic solvents (Fig. 7).

Using wet chemical methods, heteroatoms have also been doped on 3D graphene gels, having a large surface area and macroporous structure.[94,95,100,101] For example, Wu *et al.* employed ammonia boron trifluoride ($NH_3BF_3$) for the co-doping of B and N.[101] The simultaneous reduction and self-assembly of GO sheets under the hydrothermal condition

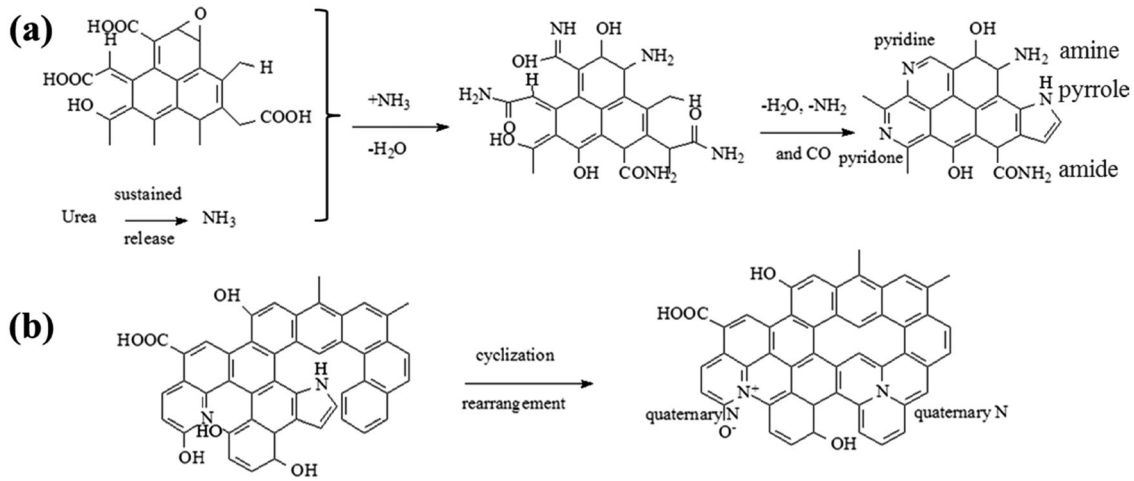


Fig. 6 Schematic illustration of (a) nitrogen insertion routes in GO. (b) Routes for the formation of a hypothetical structure of graphitic N in GO. Adapted with permission from ref. 91. Copyright (2012) Royal Society of Chemistry.

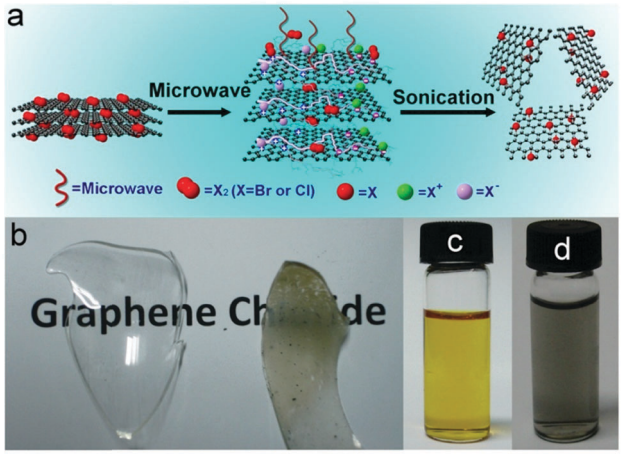


Fig. 7 (a) Synthesis of Cl- or Br-doped single-layer graphene sheets using microwave-spark method. (b) Photographs of the graphite chloride coated on the inside surface of the flask. (c and d) Photographs of Cl- and Br-doped graphene dispersion in DMF, respectively. Adapted with permission from ref. 99. Copyright (2012) Nature Publishing Group.

in addition to the subsequent freeze-drying process cause the formation of B,N-doped rGO aerogel. Solution-based doping processes also permit the simultaneous decoration of various functional nanomaterials (*e.g.* metallic nanoparticles,[102] metal oxide nanoparticles[103–107]). The doped heteroatoms facilitate the nucleation and anchoring of these nanoparticles.

**2.2.3 Other approaches.** With a short reaction time and low power consumption, plasma treatment is an effective method for heteroatom doping. Jeong *et al.* successfully achieved N doping in $N_2$ plasma (500 W in power, 14 Torr of $N_2$ gas) using $H_2$-plasma treated GO as the starting material (Fig. 8a).[108] A large number of defect sites produced from the $H_2$ plasma reduction process improve the effectiveness of N doping on the graphene basal plane. N-doping level and bonding configurations can be tuned by varying the aging time in $N_2$ plasma. The maximum N content of 2.51 at% was obtained after a 3 min plasma treatment. During the plasma process, pyrrolic N that preferably forms at the defect sites continuously increases, while graphitic N decreases and pyridinic N remains steady. $NH_3$ plasma is more reactive than $N_2$ plasma.[109,110]

However, the level of N-doping attainable by plasma treatment is generally less as compared to other doping methods. Plasma technique is particularly effective for halogen atom doping because halogen atoms are highly reactive. Wu *et al.* demonstrated plasma-assisted chlorine-doping on CVD graphene at a low power, without the generation of considerable defects.[111] A Cl coverage of 8.5 at% and conductance enhancement due to the p-doping effect were observed. By tuning the plasma conditions (reaction time, dc bias, vacuum level, *etc.*), Zhang *et al.* achieved extremely high Cl-doping of 45.3 at% (close to $C_2Cl$) on CVD graphene.[112] The C/Cl ratio and bonding states (C–Cl interaction through ionic bonding, covalent bonding, and defect creation) are sensitive to the DC bias applied.

Li *et al.* developed a photochemical method for homogeneous and patternable Cl-doping on graphene (Fig. 8b).[113] Under the xenon lamp radiation (maximum power density of 1.4 W $cm^{-2}$), chlorine molecules split into highly reactive radicals, which, in turn, covalently conjugate to the basal carbon atoms of graphene. Homogeneous doping ($\sim$8 at%) was verified by Raman mapping. Interestingly, doped-graphene becomes more transparent due to the widening of the graphene bandgap.

The arc-discharge approach is another technique to create reactive heteroatom radicals for graphene doping. Li *et al.* prepared N-doped multi-layered graphene sheets (1 at%) by DC arc-discharge using $NH_3$ as the buffer gas.[114] $NH_3$ not only acts as a N precursor but also suppresses the formation of fullerenes by terminating the edge-sited dangling C bonds with the decomposed reactive hydrogen. In addition to $NH_3$, $H_2$ along with $B_2H_6$, boron-stuffed graphite and $H_2$ along with pyridine have also been utilized as the heteroatom precursors in arc-discharge processes for the synthesis of B- and N-doped graphene (but with low doping levels $<3$ at%).[115] Shen *et al.* developed a direct-current arc-discharge method for the

 

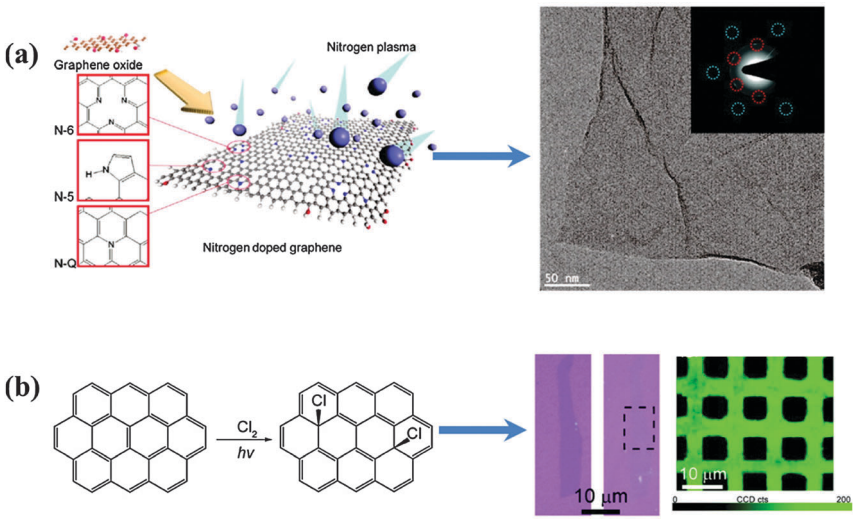


Fig. 8 (a) Schematic illustration of nitrogen plasma doping process with possible N configurations (left side); a high-resolution TEM image (right side) and selected area electron diffraction (inset) of the N-doped graphene indicate that the intrinsic layered structure and original honeycomb-like atomic structure were preserved during the plasma process. Adapted with permission from ref. 108. Copyright (2011) American Chemical Society. (b) Scheme of the photochemical chlorination process (left); optical images of a single-layer graphene sheet before and after photochemical chlorination, respectively (right, blue color); D band mapping ($\lambda_{ex}$ = 514.5 nm) of CVD-grown graphene film after patterned photochlorination (right, green colour). Adapted with permission from ref. 113. Copyright (2011) American Chemical Society.

preparation of F-doped multilayered graphene sheets.[116] A hollow graphite rod filled with powdery graphite fluoride was used as the anode and a discharge current of 140 A was applied. The resultant F-graphene is super-hydrophobic containing ~10 wt% fluorine. While dealing from low doping levels and difficulty in obtaining single-layered doped graphene, the feasibility for the mass-production and preservation of high crystallinity of graphene are the main advantages of arc-discharge techniques.

## 3 Properties of heteroatom-doped graphene

The invasion of heteroatoms into the perfect hexagonal carbon sheet of pristine graphene will inevitably cause structural and electronic distortions, leading to alterations (sometimes drastically) of graphene properties, including thermal stability, charge transport, Fermi level, bandgap, localized electronic state, spin density, optical characteristics, and magnetic properties. Depending on the type of dopants (with particular valence and size) and their bonding configurations, new or improved properties may arise and be beneficial for particular applications. A good understanding on how graphene properties can be tailored by heteroatom doping is critical for researchers to design and discover novel functionalities of graphene materials, and therefore, further extend the range of their applications.

### 3.1 Group IIIa element (B)

Boron ($2s^2 2p^1$), which is the neighboring element to carbon ($2s^2 2p^2$) with only one less valence electron, is highly amenable for graphene doping. In-plane substitutional doping (*i.e.* in-plane $BC_3$) is the most stable when compared with out-of-plane bonding (Fig. 9a).[117] As the B atom forms $sp^2$ hybridization in the carbon lattices, the planar structure of graphene is retained. However, the charge polarization exists between neighboring C atom and electron-deficient B atom. In addition, the lattice parameters are slightly altered because a B–C bond (~1.50 Å) is longer than a C–C bond (1.40–1.42 Å) in pristine graphene.[117–119] With lower induced strain energy, homogeneous substitutional B-doping is easier to achieve when compared with in-plane N-doping.[120,121] Despite the bond length expansion, the strong B–C bond ensures minimal compromise to the excellent mechanical properties of graphene.[122] On the other hand, B-doping introduces significant destructive effect on the thermal conductivity of graphene. Only 0.75 at% of B atoms can reduce more than 60% thermal conductivity of graphene.[122] In contrast to graphitic B-doping, the bonding of B atoms at the vacant sites will create structural distortion (thus significant changes in the properties). *Ab initio* DFT/GGA-simulations were performed to study the situation of filling a divacancy with a B atom.[119] The results suggest a new type of structural rearrangement—a symmetric disposition with a tetrahedral-like $BC_4$ unit, wherein all the dangling carbon atoms are saturated (Fig. 9c). Such special fourfold coordination configuration distorts the planar structure of graphene.

Heteroatom doping offers possibilities for tailoring the electronic properties of graphene. The electron-deficient nature of B induces a p-doping effect accompanied with a downshift of the Fermi level towards the Dirac point (Fig. 9b).[117] It has been predicted that the Fermi level decreases to ~0.65 eV with 2 at% graphitic B and even more at higher doping levels.[121] Scanning tunneling microscopy (STM) and theoretical simulations show that B-doping pulls more density of states (DOS) above the Fermi level because of the hole-doping effect.[118,123] It has been

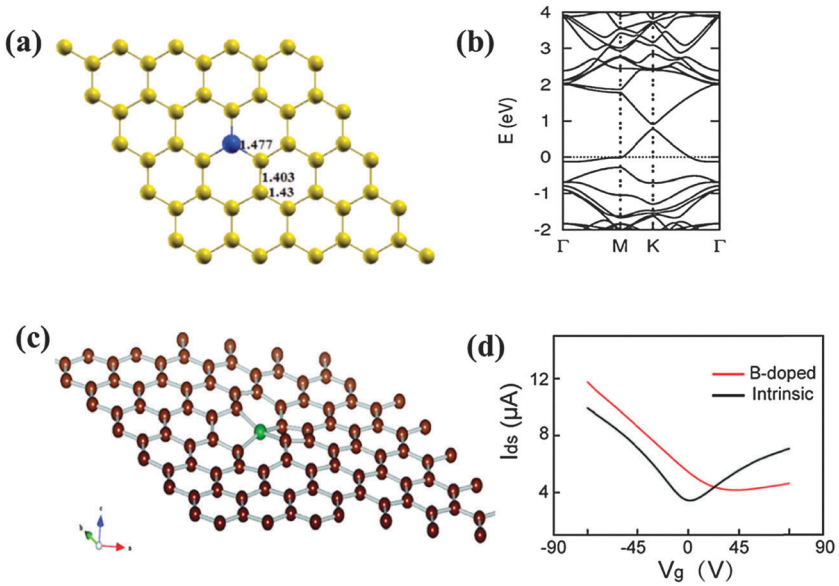


Fig. 9 (a) Substitutional doping of B (blue ball). (b) Band structure of a single B atom doped graphene sheet. Adapted with permission from ref. 117. Copyright (2013) Royal Society of Chemistry. (c) B atom in a divacancy with symmetric disposition. Adapted with permission from ref. 119. Copyright (2010) American Chemical Society. (d) Source-drain current ($I_{ds}$) *vs.* back gate voltage ($V_g$) with $V_{ds}$ = 0.1 V of B-doped (red) and pristine (black) graphene device. Adapted with permission from ref. 36. Copyright (2010) Wiley Publishing Group.

shown theoretically that a bandgap of 0.14 eV can be introduced by doping a B-atom into a 50-C-atom matrix, transforming graphene from a semimetal to a semiconductor.[117,124] The symmetry breaking in the carbon lattice is believed to be responsible for the bandgap opening, which is maximized when the B-atoms are located at the same sublattice positions. Bandgap opening is also sensitively dependent on the doping concentration and the graphene thickness (number of layers).[117,125] First-principles calculations show that B or N substitution almost does not change the linear dispersion of the electronic bands within 1 eV of the Fermi level (Fig. 9b), meaning that B- or N-doped graphene inherits some intrinsic electronic properties of graphene.[117,121] However, the anisotropy caused by B-doping is not sufficient to induce localized states, and thus magnetism.[119]

As shown by a theoretical study, the remarkable transport properties of graphene are preserved even at a high substitutional B/N doping level of 4.0 at%.[126] However, the mobility of electrons and holes (and therefore, the conductivity) becomes asymmetric with respect to the Dirac point. This is supported by the experimental observation that B-doped CVD-graphene exhibits high carrier mobility of 800 $cm^2\ V^{-1}\ s^{-1}$ and a typical p-type conductive behavior with strong asymmetry in hole and electron conduction (Fig. 9d).[36] The large Dirac point shift ($\sim$30 V) corresponds to a hole-doping concentration of $\sim 2 \times 10^{12}\ cm^{-2}$. The electrical conductivity of B/N-doped graphene increases with the dopant concentration in the low temperature region and decreases due to the elevated scattering effect from the impurity atoms in the high temperature region.[127] Considering the remarkable difference in the electronic properties between multilayer and single-layer graphene, Guillaume *et al.* investigated the influence of asymmetric substitutional B/N doping on bilayer graphene.[128] A smaller doping-induced Fermi level shift is observed in the bilayer because electrons and holes are shared by the neighboring carbon layers.

### 3.2 Group Va elements (N and P)

N is also a neighboring element to carbon in the periodic table. The electron-rich nature of N ($1s^2 2s^2 2p^3$) makes N-doped graphene distinctly different from B-doped graphene. The possible bonding configurations of N dopants are shown in Fig. 10a.[129] As discussed in the Synthesis Methods section, mainly three N bonding configurations exist, *i.e.*, graphitic (or quaternary), pyridinic and pyrrolic N. Because of the similar bond lengths of C–N (1.41 Å) and C–C (1.42 Å), pyridinic and graphitic N exert a marginal influence on the graphene structure. In contrast, $sp^3$ bonded pyrrolic N disrupts the planar structure of graphene.[130] Pyridinic N bonding configuration is the most stable in the presence of monovacancy, while pyridinic and graphitic N dominate in the presence of Stone–Wales and divacancy defects.[131,132]

The larger electronegativity of N (3.04 on the Pauling scale) than that of C (2.55 on the Pauling scale) creates polarization in the carbon network, thereby influencing the electronic, magnetic and optical properties of graphene.[133] N-doping opens a bandgap near the Dirac point by suppressing the nearby density of states (DOS), thereby conferring graphene with semiconducting properties (Fig. 10b).[134,135] The semiconducting behavior of N-doped graphene depends on the doping configurations. For graphitic N, three valence electrons of nitrogen form three σ-bonds with the neighboring carbon atoms, one electron is engaged in a π bond formation, and the fifth electron is partially involved in the π*-state of the conduction band. Each graphitic N can contribute $\sim$0.5 electron to the π network of the graphene lattice, resulting in an

 

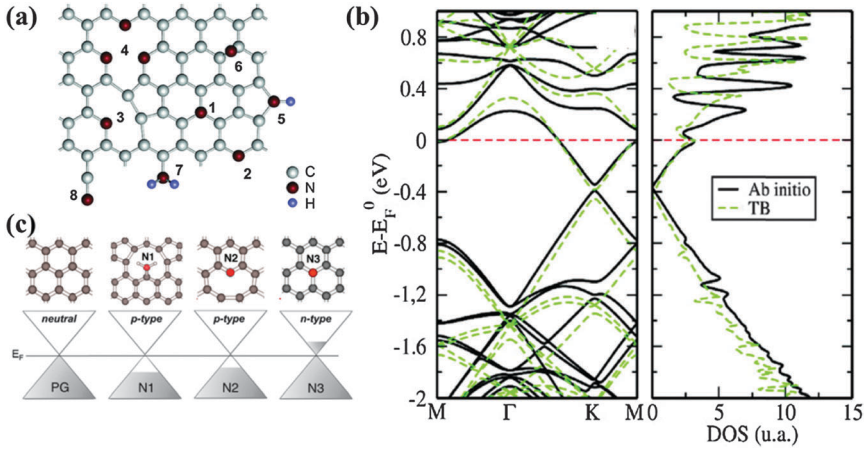


Fig. 10 (a) Possible configurations of nitrogen dopants in graphene: 1-graphitic N, 2-pyridinic N, 3-single N pyridinic vacancy, 4-triple N pyridinic vacancy, 5-pyrrolic N, 6-interstitial N or adatom, 7-amine, 8-nitrile. Adapted with permission from ref. 129. Copyright (2011) American Chemical Society. (b) *Ab initio* (thick black lines) and tight-binding (green dashed lines) band structures (left) and DOS (right) of a 10 × 10 graphene supercell containing one substitutional N dopant. Adapted with permission from ref. 134. Copyright (2013) American Chemical Society. (c) Computed doping effect of N dopant for the different bond types as compared to pristine graphene. Adapted with permission from ref. 137. Copyright (2012) American Chemical Society.

n-doping effect.[136] In comparison, pyridinic and pyrrolic N form at the defects sites, and these defects impose the p-doping effect by withdrawing electrons from the graphene sheet (Fig. 10c).[137]

Liu *et al.* demonstrated graphitic N-dominated CVD-graphene with n-type behaviour and carrier mobility of 200–450 $cm^2\ V^{-1}\ s^{-1}$.[135] Li *et al.* further reported crossover behaviour from the p-type to n-type with an increasing N-doping level: even the dominant species are pyridinic and pyrrolic types.[138] Schiros *et al.* attributed this phenomenon to the hydrogenation of pyridinic and pyrrolic N, which transformed them from the p to n type.[137] Usachov *et al.* reported a bandgap opening of ~0.3 eV and charge-carrier concentration of $\sim 8 \times 10^{12}\ cm^{-2}$ induced by the 0.4 at% doping of graphitic N.[129] Sodi *et al.* theoretically showed that in contrast to doping at the basal plane, edge functional groups exert a marginal influence on the band structure of graphene.[139] As shown by Ouerghi *et al.*, only 0.6 at% graphitic N-doping results in a large carrier concentrations of $2.6 \times 10^{13}\ cm^{-2}$ (4 times higher than that of pristine graphene), while pyridinic and pyrrolic N exert little influence.[140]

N doping has also been proven to be powerful in tuning the work function of graphene materials, which is instrumental for devices such as organic field effect transistors (OFETs) and light emitting diodes (LEDs). Schiros *et al.* calculated the work function of pristine graphene (4.43 eV) and graphene doped with graphitic (3.98 eV), pyridinic (4.83 eV), and hydrogenated pyridinic (4.29 eV) N.[137] The change of the work function is caused by the electron donating or accepting nature of each N-bonding configuration. Consistently, Kim and co-workers confirmed the reduction of the work function by graphitic N-doping using ultraviolet photoelectron spectroscopy.[141] Contradictory to the theoretical predication, Lin *et al.* showed that pyridinic N reduces the work function of CVD graphene.[142] This discrepancy could be due to the hydrogenation of pyridinic N.[137]

More recently, the creation of a magnetic moment on graphene by heteroatom doping has attracted considerable research interest for spintronic applications. Due to the lack of nonbonding electrons, graphitic N is not able to generate a magnetic moment. Although both pyrrolic and pyridinic N have a non-bonding electron pair, only pyrrolic N can form π and π* states that lead to spin polarization. Therefore, pyrrolic N can create strong magnetic moments, while pyridinic N only has a weak effect.[143] Furthermore, Chen *et al.* theoretically demonstrated that each pyrrolic N doped at the edge sites of graphene nanoribbons (GNR) produces a magnetic moment of 0.95 $\mu_B$, while pyridinic N at the edges creates a magnetic moment of 0.32 $\mu_B$.[144]

N doping can also tailor the optical properties of graphene sheets. Chiou *et al.* demonstrated the influence of N-doping on the photoluminescence (PL) property of graphene nanoflakes (GNF).[145] When excited, the electrons of doped N can transfer energy to the π* state of the $sp^2$ cluster of GNF. Therefore, a larger amount of energy is released when electrons fall from the π* state back to the π state, leading to higher intensity PL (Fig. 11). As demonstrated by Kim *et al.*, pyrrolic, pyridinic and graphitic N result in the blue-shift of the PL peak, while only graphitic N is able to enhance the intensity.[146] However, Tang's group reported that with 3.05 at% pyridinic-N, the PL emission of rGO is quenched by 76%, possibly because of the intramolecular energy transfer between the doped N and graphene sheet.[147]

As P is larger than N, P-doping causes more structural distortion. By transforming the $sp^2$ hybridized carbon into the $sp^3$ state, P can form a pyramidal like bonding configuration with three carbon atoms. In such a configuration, P overhangs from the graphene plane by 1.33 Å accompanied with 24.6% increase in the P–C bond length with respect to the C–C bond length of pristine graphene (Fig. 12a).[148] Unlike N, the electronegativity of the P atom (2.19) is significantly lower than that of

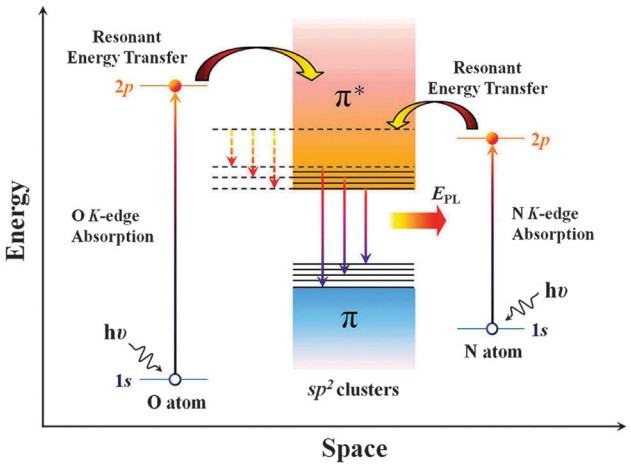


Fig. 11 Possible mechanism of photoluminescence enhancement by resonant energy transfer from N and O dopants to the $sp^2$ clusters in the GNFs matrix. $E_{PL}$ stands for the enhanced PL emission. Solid and dotted lines represent radiative ($E_{PL}$) and nonradiative (low and broad PL) relaxation processes, respectively. Adapted with permission from ref. 145. Copyright (2012) American Chemical Society.

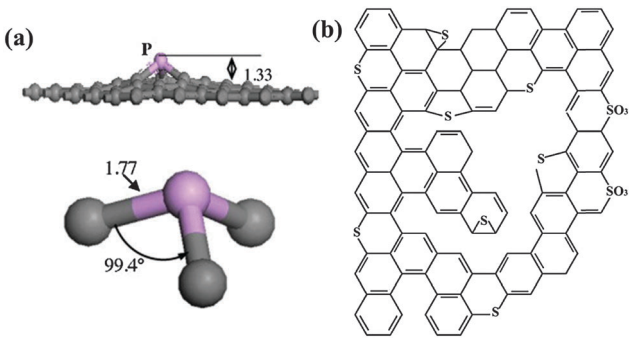


Fig. 12 (a) Optimized geometrical structure of P-doped graphene. The gray and pink balls represent the carbon and phosphorus atoms, respectively. The bond distances are in angstroms. Adapted with permission from ref. 148. Copyright (2013) Elsevier Publishing Group. (b) Typical configuration of S-doped graphene. Adapted with permission from ref. 82. Copyright (2012) American Chemical Society.

the C atom (2.55);[149] therefore, the polarity of the C–P bond is opposite to that of the C–N bond. Further, when compared with N-doping, distinct effects by P-doping may also arise from the additional orbital of P ($3s^2 3p^3$).

Hirshfeld population analyses show that P can transfer 0.21*e* to the graphene sheet[148] and graphitic N transfers 0.5*e*, suggesting the stronger ability of N for electron donation.[150] Contrarily, it has been shown that P-doped bilayer graphene exhibits prominent n-type behaviour with 5 times higher electron mobility than pristine bi-layer graphene, while N-doped bi-layer graphene shows a weaker n-type behavior and lower mobility than pristine graphene.[151] The same study also shows that unlike N-induced n-doping, the n-type behavior of P-doped graphene is retained in the oxygen atmosphere. The discrepancy between the theoretical prediction and experimental observation may be because N-doping from graphitic N is partially neutralized by the co-existing electron-accepting pyridinic and pyrrolic N.

A theoretical investigation suggests that the bandgap opening positively depends on the P-doping concentration, and a bandgap of 0.3–0.4 eV is resulted with a P-doping level of 0.5 at%.[152] Similar to N-doping, P-doping can also induce a magnetic moment. Zhao *et al.* found that the magnetic moment of P-doped graphene is $\sim$1.02 $\mu_B$ due to the symmetry breaking of the graphene π-electron framework.[148] This value is in good accordance with the DFT calculations (1.05 $\mu_B$) reported by Dai and Yuan.[153] P-doping is more potent than N-doping in inducing magnetic moments.

### 3.3 Group VIa elements (O and S)

VIa group is also known as the oxygen family, among which, oxygen is the most electronegative element. The substitutional doping of an O atom is impossible because of its strong electronegativity and large size. Graphene oxide (GO), usually oxidatively exfoliated from graphite powder, is the most studied graphene derivative. Having epoxyl (C–O–C) and carbonyl (C═O) groups, GO and its reduced form (rGO) can be regarded as O-doped graphene. The covalent attachment of oxygen groups transforms $sp^2$ into the $sp^3$ hybridization state, accompanied by local distortions of the graphene planar structure. The extensive presence of localized $sp^3$ domains gives rise to a bandgap opening,[154,155] and together with the defects, they make GO poorly conductive or non-conductive. Excellent hydrophilicity makes GO suitable for solution processes.

It is generally assumed that a GO sheet bears hydroxyl and epoxyl groups on its basal plane and carboxyl and carbonyl groups at the edges.[156] As a non-stoichiometric compound, the properties of GO highly depend on the abundance and composition of different types of oxygen groups, which are specific to synthetic processes and post-synthesis treatments.[13,157] Intriguingly, the chemistry of GO changes in the ambient condition, for example, epoxyl groups may evolve to hydroxyl groups in the presence of hydrogen.[158–160] The acidic and oxidative nature of abundant oxygen functionalities allow GO to function as a mild and green oxidant and catalyst. For example, GO has been reported to be capable of oxidizing substituted *cis*-stilbenes to their corresponding diketones and facilitating an oxygen activation reaction.[161–163] As GO and rGO have already been thoroughly discussed in a number of review articles,[13,164,165] in this article, we emphasize more on other heteroatom doping.

S shares similar doping configurations as O, *e.g.*, C–S–C, C–$SO_x$–C ($x$ = 2, 3, and 4) and C–SH (Fig. 12b).[82] The C–S bond length (1.78 Å) is $\sim$25% longer than that of the C–C bond.[166] Consequently, a curved carbon nanostructure (*e.g.*, carbon nanotube) favors S-doping more than flat graphene. A theoretical study has proposed that S-doping on graphene occurs in two steps: the formation of defect sites and S═S bond rapture, and depending on the doping level, the resultant graphene sheet can become a small-band-gap semiconductor or more metallic than pristine graphene.[167] Poh *et al.* experimentally measured the resistivity of S-doped graphene thermally exfoliated from graphite oxide in the presence of S-precursor.[78] In general,

 

S-doped graphene is more resistive than pristine graphene because of the free carrier trapping caused by sulfur and oxygen functionalities.

Unlike B, N, and P, negligible polarization (or charge transfer) exists in the C–S bond because of the similar electronegativity of S (2.58) and C (2.55).[168] On the other hand, in contrast to the zero spin density of pristine graphene, the mismatch of the outermost orbitals of S and C induces a non-uniform spin density distribution on S-doped graphene, which consequently endows graphene with catalytic properties useful for many applications (*e.g.*, oxygen reduction reaction, ORR).[82,83] Using first-principles calculations, Jeon *et al.* found that covalently bonded S and oxidized S at both the zigzag and armchair edges of graphene nanoplates (SGnPs) obtained from ball milling can induce a significant spin density increase.[82] In addition, the oxidization of SGnPs further enhanced their catalytic activity, accompanied by 5–10 times increase of magnetic moments. The same study also showed that the highest occupied molecular orbital (HOMO) and lowest unoccupied molecular orbital (LUMO) of graphene are strongly polarized by edge-sited S dopants, leading to high catalytic activity towards ORR. In contrast to the extensive studies on O- and S-doping, there are only a few reports on Se-doping.[80] The properties of Se-doped graphene remain largely unexplored.

### 3.4 Group VIIa elements (F, Cl, Br and I)

As is well known, halogens possess higher reactivity than group IIIa–VIa elements. As halogen-doping transforms $sp^2$ carbon bonding to the $sp^3$ state, it results in drastic distortions in the geometric and electronic structures of graphene. As F is one of the most reactive elements, F-bonding is strong and inert. The F–C bond in F-doped graphene sticks out the basal plane (Fig. 13a),[111] and it stretches the C–C bond length to 1.57–1.58 Å.[169] First-principles calculations suggest that the high affinity of F towards C enables the negative chemisorption energy of F on graphene even at the full coverage of F atoms ($[CF]_n$, which is called fluorographene).[170] For fluorographene, F is covalently bonded to $sp^3$ C, and the graphene sheet is buckled as the F attachment alternates on both the sides of the graphene sheet (*i.e.*, basal plane is sandwiched by two F-layers). Fluorographene has attracted a great deal of attention because of its extraordinary mechanical strength, high thermodynamic stability and superb chemical inertness.[169,170] These properties promise the use of fluorographene, for example, as a lubricant and battery additive. Fluorographene is the thinnest insulator because of its wide bandgap of ~3 eV, resulting from a high degree of $sp^3$ bonding of carbon atoms (Fig. 13b).[169,171,172]

F-doped graphene can be employed as semiconductors with a bandgap tunable by the F-coverage[98] and with luminescence ranging broadly from the ultraviolet to visible light regions.[173] Obtained by exposing only one-side of CVD graphene to xenon difluoride, single-sided F-doped graphene (25% F coverage, $C_4F$) is optically transparent with a bandgap of 2.93 eV and over 6 orders of increase in resistance when compared with pristine graphene.[171] Further, F-doping increases the hydrophobicity of graphene.[116]

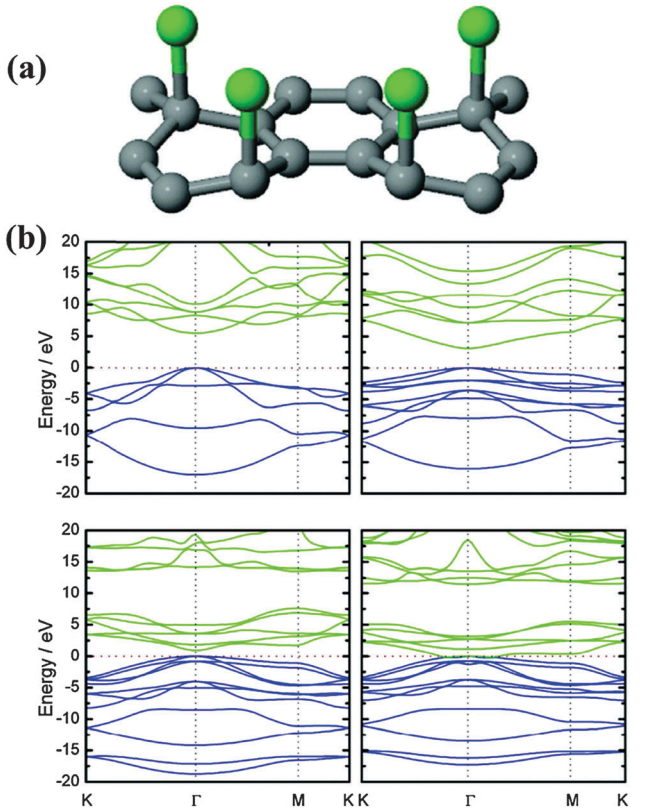


Fig. 13 (a) Schematic illustration of partially fluorinated or chlorinated graphene structure. Adapted with permission from ref. 111. Copyright (2011) American Chemical Society. (b) The electronic band structure of CH, CF, CCl, and CBr along lines connecting the high-symmetry points *K*, *Γ* and *M* in the Brillouin zone. The zero-energy level has been set to the valence band maximum. Adapted with permission from ref. 169. Copyright (2010) Wiley Publishing Group.

In the case of Cl-doped graphene, *ab initio* simulations show that Cl atoms on graphene have a lower binding energy and longer bond length than that of F and H, suggesting that the covalent Cl–C bond is less stable than C–F and C–H bonds (Fig. 14a–c).[111] Because of the long bond length, Cl-doped graphene (1.1–1.7 nm) is thicker than F-doped graphene.[113] In addition to the similar bonding arrangement as F (Fig. 13a), Cl can interact with C *via* forming charge-transfer complex, covalent bonding, and physical absorption as suggested by DFT calculations.[130] Further, 25% coverage of covalently bonded Cl ($C_4Cl$) creates a bandgap of 1.4 eV. At full coverage of Cl, Br and I, non-covalent interaction is more stable.[174,175] The full coverage of Cl (like fluorographene) is controversial. It has been theoretically proposed that alternative covalent bonding on both the sides allows full Cl coverage: even at full coverage, the graphene bandgap is only opened to ~1 eV (Fig. 13b).[169] However, Sahin *et al.* reported that the dense decoration of Cl on a graphene surface leads to the desorption of Cl in the form of $Cl_2$ due to a stronger Cl–Cl interaction.[176]

Cl is a p-dopant (Fig. 14d). Zhang *et al.* successfully synthesized Cl-doped graphene with a high Cl coverage of 45.3% (close to $C_2Cl$), which was stable over one week under ambient conditions.[112] Hall-effect measurements reveal the p-doping

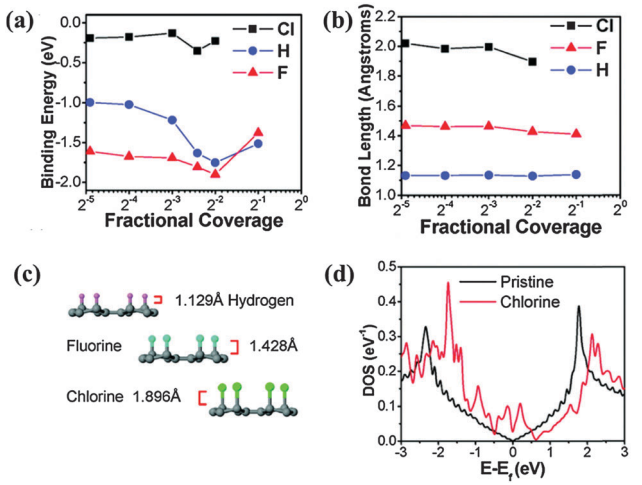


Fig. 14 (a) Binding energies and (b) bond lengths of the C–X bond (X = Cl, H, F) as functions of coverage, based on *ab initio* simulations. (c) Atomistic structures and bond lengths of C–X. (d) Calculated DOS of graphene with a 1/30 coverage of Cl atoms in comparison with that of pristine graphene as a function of energy $E - E_F$, where $E_F$ is the Fermi energy. Adapted with permission from ref. 111. Copyright (2011) American Chemical Society.

effect and a high hole concentration of $1.2 \times 10^{13}$ $cm^{-2}$ (increase of ~3 times) (Fig. 15). In comparison with the carrier mobility decrease of F-doped graphene from 1060 $cm^2$ $V^{-1}$ $s^{-1}$ to about 5 $cm^2$ $V^{-1}$ $s^{-1}$,[171] Cl-doping preserves a high carrier mobility of 1535 $cm^2$ $V^{-1}$ $s^{-1}$.[112] In addition, Cl-doping enhances the conductivity of graphene by 2 times (Fig. 15). Owing to the low binding energy, Cl-doping and Br-doping start to decompose at a low temperature (<400 °C) and completely evaporate at a temperature of >600 °C.[99]

In contrast to the extensive research efforts spent on F- and Cl-doping, there are only a few theoretical and experimental reports on Br- or I-doped graphene. This is due to the thermodynamic instability correlated with their large sizes and low electronegativity (F = 3.98, Cl = 3.16, Br = 2.96 and I = 2.66). Unlike F and Cl, large-sized halogen atoms (Br and I) are likely to interact with graphene only *via* physisorption or charge-transfer complex formation, without disrupting the $sp^2$ carbon network.[174,177] As shown in Fig. 13b, brominated graphene is an indirect gap material with almost zero bandgap. In comparison, hydrogenated, fluorinated and chlorinated graphene materials are direct bandgap materials.[169] Further, DFT studies reveal the metallic behaviors of Br- or I-doped graphene materials.[169,174] The electronegative and chemically reactive properties of I facilitate its easy aggregation to form linear polyiodide anionic species (*e.g.* $I_3^-$ and $I_5^-$) on the graphene surface.[46,85]

### 3.5 Other dopants

Graphene hydrogenation *via* $sp^3$ C–H bond can transform zero bandgap graphene into a wide-gap semiconductor.[178,179] Many studies have been conducted on the structural, electronic and magnetic properties of fully or partially hydrogenated graphene.[180–182] However, because of the small difference in the electronegativity between C and H, the C–H bond is essentially non-polar,

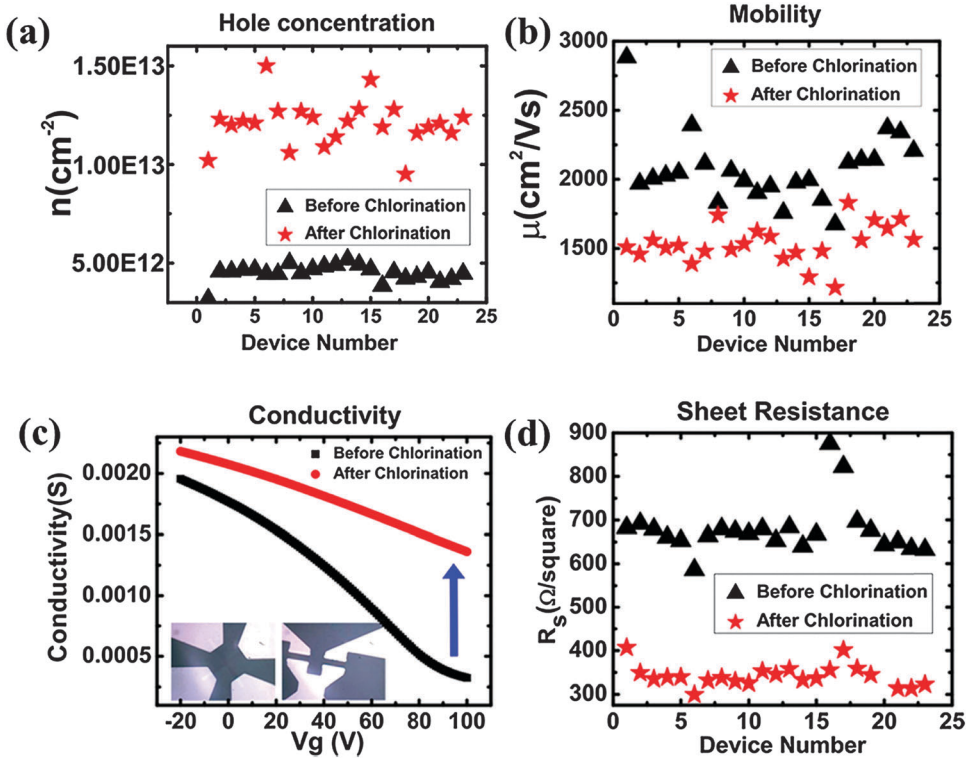


Fig. 15 Chlorination changes the transport properties of graphene. (a) Carrier concentration. (b) Mobility. (c) Electrical conductivity. (d) Sheet resistance. Adapted with permission from ref. 112. Copyright (2013) American Chemical Society.

 

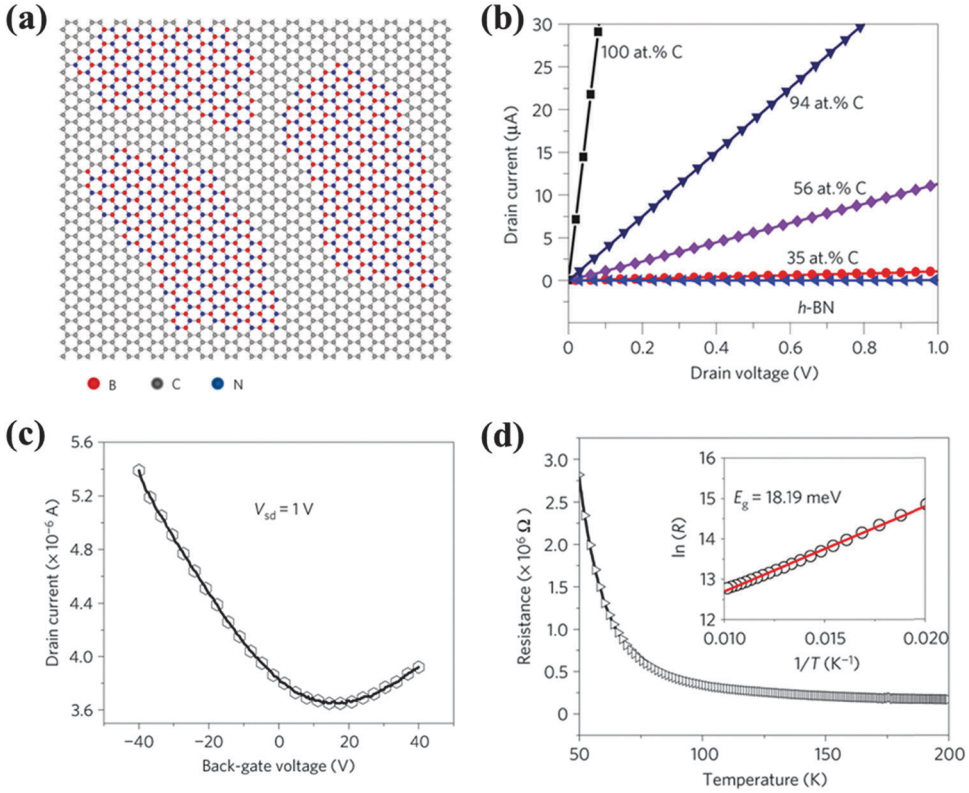


Fig. 16 (a) Atomic model of the *h*-BNC film showing hybridized *h*-BN and graphene domains. Scale bars: 2 nm. (b) Current–voltage (*I*–*V*) characteristics of as-grown BNC with different percentages in carbon measured at room temperature. (c) The drain current as a function of the voltage applied to the back gate for a 7 μm-wide BNC ribbon with 40% carbon. The drain–source voltage is fixed to 1 V. (d) Resistance *vs.* temperature curve for a typical *h*-BNC ribbon with a width of 5 μm and a length of 11 μm. The inset shows ln(*R*) as a function of $T^{-1}$ in the temperature range from 50 to 100 K. Adapted with permission from ref. 33. Copyright (2010) Nature Publishing Group.

and therefore, non-reactive. This largely limits the practical applications of hydrogenated graphene materials.

The doping of metallic atoms has rarely been demonstrated experimentally. This is probably because the binding energy between these elements with graphene is much lower than their cohesive energy. Consequently, they tend to form clusters instead of being uniformly doped on the graphene surface.[183] In addition, large-sized metal atoms can create a larger local curvature, favoring the chemisorption of small molecules from the ambience (*e.g.*, $H_2O$, $O_2$, NO), which greatly limits the practical applications of such doped graphene.[184,185]

Silicon (Si), which belongs to the same group as C, is a tetravalent metalloid. The much longer bond length of Si–C (1.75 Å) with respect to the C–C bond forces the Si atom to protrude from the graphene plane, accompanied with remarkable distortion of the graphene planar structure. The created disorders make Si-doped graphene promising as a metal-free catalyst for CO oxidation,[186] ORR,[187] NO and $NO_2$ reduction.[188,189] However, the experimental reports on Si-doped graphene are rare. This may, at least in part, be attributable to the strong chemisorption of the ambient molecules,[190] which unavoidably change the intrinsic properties of Si-doped graphene.

### 3.6 Co-doping

The co-doping of multiple species of foreign atoms may generate new properties or create synergistic effects. B and N atoms are similar in size and produce opposite doping effects on graphene. While being simultaneously doped onto graphene, boron nitride (BN) domains tend to form due to the phase separation between C and BN (Fig. 16a).[33,191–194] This is attributed to the larger binding energy of B–N and C–C than that of B–C and N–C bonds. B,N co-doping leads to four bonding configurations, *i.e.* C–C, B–N (dominating form), C–B and C–N with bond lengths of 1.42 Å, 1.45 Å, 1.49 Å and 1.35 Å, respectively.[193] Strong charge polarization exists between B and N,[193,195] which yields active surface chemistry. The thermal stability of B,N co-doped graphene is lower than N-doped graphene, but higher than B-doped graphene.[35]

The co-doping of B and N on graphene by CVD produces a $sp^2$ hybridized hexagonal lattice with BN domains (B/N ratio = 1) surrounded by graphitic domains.[33] The conductivity of such films (*h*-BNC) is tunable from insulating to highly conductive depending on the C percentage (Fig. 16b). Similar to previously reported $BC_2N$ thin-film,[196,197] *h*-BNC exhibits a p-type semiconducting behavior with electron and hole mobility of 5–20 $cm^2\ V^{-1}\ s^{-1}$ (Fig. 16c). The reduced mobility is attributed to the electron scattering at the boundaries between BN and C domains. Based on the temperature-dependent resistivity of *h*-BNC (with 56 at% C), a small bandgap (18 meV) is predicted (Fig. 16d). Asymmetric B,N doping ($B_{7.8}N_{4.7}C_{87.5}$) moderately increases the bandgap (0.49 eV) because of symmetry breaking.[198]

It has been shown that at an appropriate B/N ratio, the HOMO–LUMO energy gap of graphene may be reduced, leading to enhanced chemical reactivity.[69] Both B and N doping creates a bandgap at the Dirac point, but they shift the Fermi level in opposite directions. Uniform B,N co-doping (although it is difficult to experimentally realize) is believed to open a bandgap at the Dirac point without shifting the Fermi level.[193,199,200] As suggested by DFT studies, the opened bandgap increases with the size of the BN domains, regardless of their shapes.[195]

In contrast, random and scattered distribution of foreign atoms is observed in the case of S,N or P,N co-doping.[45,201] Crosstalks between the co-dopants may affect their bonding configurations. For example, the co-doping of P may promote the pyridinic bonding of N on graphene.[201] Pyrrolic N dominates in N-doped graphene, whereas the co-doping of S makes graphitic N dominant.[45]

# 4 Applications

Doping by a range of heteroatoms with varying configurations and doping levels endows graphene with a wide spectrum of new properties, for example, bandgap opening, charge polarization between heteroatom and C atom, magnetic moment, hydrophilicity, increased spin density, catalytic activities, *etc.* Doped graphene materials are, therefore, useful for various applications including energy storage, energy conversion, sensing, and gas storage (Table 2).

## 4.1 Supercapacitors

Due to their high power density and long lifecycle, supercapacitors have been intensively researched as energy storage devices. Graphene, which has the highest specific surface area, offers large electric double-layer capacitance (EDLC). However, chemically inert pristine graphene is not able to provide electrochemical capacitance (pseudocapacitance). Hence, doped graphene materials are promising for supercapacitors because of the preserved large EDLC, improved wettability, and existence of pseudocapacitance.[202]

It has been shown that the abundant oxygen groups on rGO enhance its specific capacitance to 189 F $g^{-1}$.[203] When compared with O-doped graphene, graphene materials doped with B, N and P are more advantageous because of their better conductivity, stability, chemical reactivity, and sheet-to-sheet separation. A porous B-doped graphene structure synthesized by annealing frozen GO–boric acid composite shows a specific capacitance of 281 F $g^{-1}$.[60] N-doped graphene hydrogel (5.86 at% N with dominant pyrrolic N) synthesized by the hydrothermal method yields a large specific surface area of $\sim$1500 $m^2$ $g^{-1}$ and a high specific capacitance of 308 F $g^{-1}$.[100] The same study also showed that the capacitive performance of N-doped graphene not only depends on the N content but also on the doping configurations. Graphitic and pyridinic N can improve the wettability of doped graphene because of their large dipole moments. Further, graphitic N can facilitate electron transfer, thereby improving the capacitive behavior by lowering the charge-transfer resistance of the electrode at a high current density.[108,204] Being electrochemically active in an alkaline aqueous solution, pyridinic and pyrrolic N offer high pseudocapacitance.[100] At optimized balancing in N bonding configuration and doping level, a hydrothermally synthesized N-doped graphene (10.13 at%) achieves a specific capacitance of 326 F $g^{-1}$ and excellent cycling stability (99.85% columbic efficiency after 2000 cycles).[205]

Jeong *et al.* fabricated a N-doped graphene-based flexible (wearable) supercapacitor that exhibits 4 times larger capacitance

Table 2 Summary of applications of heteroatom-doped graphene

| Applications | Materials | Advantages of doping effects | Ref. |
|---|---|---|---|
| Supercapacitors | B/N/P doped graphene<br>B,N co-doped graphene<br>N-doped graphene/$MnO_2$ | Enhanced electrochemical activity; lower charge-transfer resistance; better sheet-to-sheet separation; improved conductivity than GO precursors. | 203, 206 and 207<br>101<br>211 |
| Lithium ion batteries | B/N/P doped graphene<br>N,S co-doped graphene<br>N doped graphene–$SnO_2$/MnO/$TiO_2$/$VO_2$/$Zn_2GeO_4$/α-$Fe_2O_3$ | Achieving balance between Li binding and diffusion; enable abundant and uniform loading of metal oxide nanoparticles. | 59 and 224<br>225<br>106, 226–230 |
| Fuel cells (cathode for ORR and anode of DMFC) | B/N/P/S/halogen doped graphene<br>N,B/N,P/N,S co-doped graphene<br>N doped graphene–Pt NW/PtRu | Induced charge polarization and spin density enhances oxygen adsorption and cleavage; enable abundant and uniform loading of metal nanoparticles. | 43–47, 51 and 53<br>69, 80 and 201<br>81 and 251 |
| Solar cells (DSSC and heterojunction solar cell) | B/N/F doped graphene | Increases the catalytic activity of DSSC counter electrode; endows graphene with p or n doping effect; increases graphene work function. | 32, 254 and 257 |
| Sensors (electrochemical, electronic and SERS sensors) | B/N/P/Si/S doped graphene<br>B,N/S,N/Si,N co-doped graphene | Facilitates charge transfer, analyte adsorption and activation; assists anchoring of functional moieties or molecules; opens graphene bandgap; induces charge polarization. | 39, 262, 263, 269 and 275<br>261, 266 and 272 |
| Gas storage | B/N doped graphene | Increases binding affinity towards gas molecules; enables abundant and uniform loading of metal nanoparticles. | 277, 281 and 282 |

 

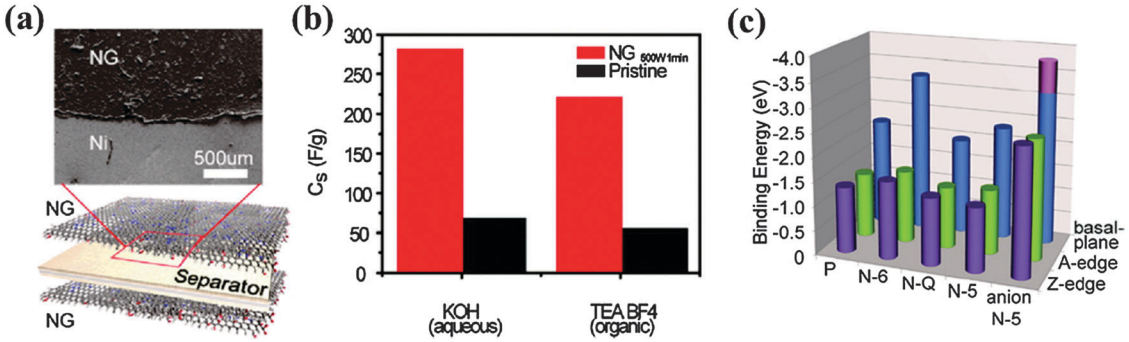


Fig. 17 Ultracapacitors based on N-doped graphene and their electrochemical testing. (a) A schematic illustration of the assembled supercapacitor structure alongside a scanning electron microscopy image, showing the top view of the device. (b) The specific capacitances measured in aqueous and organic electrolytes. (c) The binding energies between potassium ions and N-configurations at basal planes and edges, which were calculated by first-principles DFT. "P, N-6, N-Q and N-5" along the horizontal axis indicates "pristine", pyrrolic, pyridinic and graphitic N, respectively. Adapted with permission from ref. 108. Copyright (2011) American Chemical Society.

than its pristine graphene-based counterpart, in both aqueous and organic electrolytes (Fig. 17).[108] Theoretical calculations suggest that pyridinic N at the basal plane plays a major role for capacitance improvement due to its large binding energy with $K^+$. On the other hand, the strong ionic bonding between negatively charged pyrrolic, and $K^+$ is predicted to be disadvantageous for the reversible charge–discharge process (Fig. 17). Fan *et al.* synthesized a N-doped graphene (8.7 at%) hollow structure by a thermal annealing of layer-by-layer composited GO, PANI and polystyrene nanospheres.[206] Attributable to the synergistic effect of N-doping and hollow-sphere structure, it exhibits a high specific capacitance even at high current densities (381 F $g^{-1}$ at 1 A $g^{-1}$; 282 F $g^{-1}$ at a high current density of 20 A $g^{-1}$) and outstanding cycling stability (96% retention after 5000 cycles).

Rajalakshmi *et al.* prepared P-doped graphene by annealing rGO with phosphoric acid at 220 °C.[207] Working as the supercapacitor electrode in 1 M $H_2SO_4$ electrolyte, it offers a much higher capacitance (367 F $g^{-1}$ at scan rate 5 mV $s^{-1}$) than rGO control.[207] Phosphorus on graphene is believed to assume the oxidized form and produces pseudocapacitance. S- and halogen atom doping are also expected to enhance the capacitance of graphene-based electrodes. However, their practical applications in this regard are hindered by the complicated synthesis process, limited doping level and/or low yield. In addition, the pseudocapacitive behaviors from these dopants are unclear. A few S-doped activated carbon materials have been reported for supercapacitor applications, and sulfone and sulfoxide species formed have been proposed to participate in the redox faradic reactions during the charge–discharge process.[208,209]

Wu *et al.* synthesized 3D B,N co-doped graphene aerogel (BN-GA, ~0.6 at% B and ~3.0 at% N) as an additive-free monolithic composite for an all-solid-state supercapacitor (Fig. 18).[101] This electrode (with a capacitance of 239 F $g^{-1}$) outperforms the counterpart electrodes without doping or doped with only B or N because of the synergetic effects between the two co-dopants. The solid-state supercapacitor equipped with such an electrode achieves a high energy density of ~8.7 W h $kg^{-1}$ and power density of 1650 W $kg^{-1}$. O, N and Cl triply-doped rGO (16.36 at% O, 1.46 at% N mainly as pyridinic N, 1.1 at% Cl mainly as C–Cl or C–Cl═O) has been prepared by the anode polarization of rGO film in nitrogen-deaerated 1 M KCl solution.[210] These electron-rich dopants largely increase the electrode capacitance as compared with a rGO based electrode. Heteroatom doping not only enhances the capacitance of graphene materials, but also facilitates the uniform and abundant loading of pseudocapacitive metal oxides *via* serving as nucleation and anchoring sites. Yang *et al.* synthesized a composite of N-doped graphene and ultrathin $MnO_2$ sheet by the hydrothermal method and found a specific capacitance increase from 218.8 to 257.1 F $g^{-1}$ and improved the cycling stability after N-doping.[211]

### 4.2 Lithium ion batteries

Lithium ion batteries (LIB) are energy storage devices with a high energy density. However, they have a relatively low power density and poor cycling stability. Pristine graphene is not suitable for Li storage due to (1) its low binding energy towards Li atoms (hence, adsorbed Li atoms tend to cluster on the graphene surface) and (2) high energy barrier for Li to penetrate through the graphene sheet.[212,213] The existence of defects enables Li penetration and prevents Li clustering due to the strong interaction between Li and defect sites.[213,214] On the other hand, the abundant defect sites not only compromise the mechanical robustness and electrical conductivity of graphene, but also limit the lateral diffusion of Li.[215]

Heteroatom doping could be instrumental to optimally balance Li storage and diffusion for graphene-based electrodes.[216] A partial density of states (PDOS) study suggests that a Li atom as a potent electron donor is fully ionized on graphene and interacts with graphene mainly by ionic bonding.[217] Graphene substitutionally doped with B atoms is an electron-deficient system, which is desirable for improving the storage capacity of electron-donating Li.[217,218] However, the enhanced binding energy between Li and B-doped graphene limits Li diffusion (and therefore, the delithiation process).[217,219] In contrast, graphene doped with electron-rich graphitic N shows more efficient delithiation because of the electrostatic repulsion between N and Li.[212,217] However, this comes at the price of reduced Li storage capacity due to the lowered binding energy.[220]

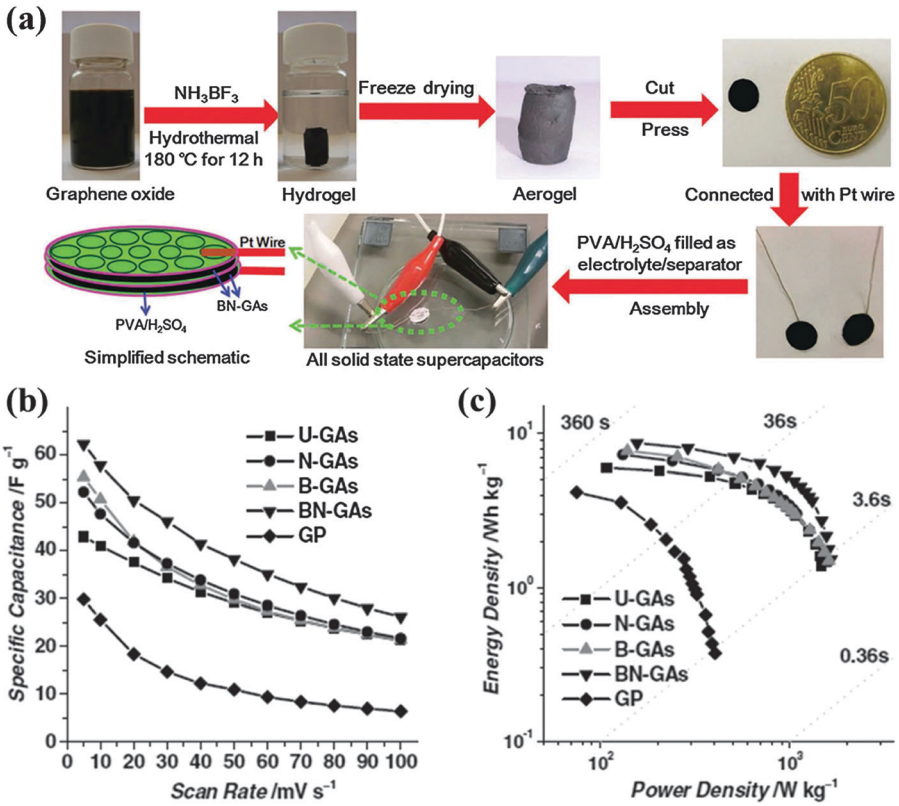


Fig. 18 (a) Fabrication of all-solid-state supercapacitor (ASSS) based on B,N-GAs that were produced by a combined hydrothermal process and freeze-drying process. (b) Specific capacitance of undoped GAs (U-GAs), N-GAs, B-GAs, BN-GAs, and graphene paper (GP) based ASSSs on the basis of two-electrode mass as a function of scan rates from 1 to 100 mV $s^{-1}$. (c) Ragone plot of ASSSs based on U-GAs, N-GAs, B-GAs, B,N-GAs and GP. Adapted with permission from ref. 101. Copyright (2012) Wiley Publishing Group.

Altogether, graphitic B doping promotes LIB capacity, whereas graphitic N doping improves the charge/discharge rate performance. Both these graphitic doping procedures are not able to enhance the penetration of Li through graphene sheets (perpendicular diffusion).[213]

Pyridinic and pyrrolic N formed at the edges and defect sites can promote the perpendicular diffusion of Li.[213,221] In addition, Cao *et al.* theoretically showed that pyridinic and pyrrolic N have a higher binding energy with Li than that with graphitic N, which is favorable for increasing the storage capacity.[216] On the other hand, the strong coulombic attraction between pyridinic/pyrrolic N and the adsorbed $Li^+$ hinders the delithiation process.[213] A theoretical study shows that N-doping at divacancy defects facilitates perpendicular penetration, while doping at both monovacancy and divacancy has the desired binding energy to optimally balance the binding capacity and delithiation of Li.[213]

Experimental investigations have been conducted to explore the potential of B- or N-doped graphene as an LIB anode. Reddy *et al.* reported a CVD-grown N-doped graphene (9.0 at%) anode that achieves a higher reversible discharge capacity (0.05 mA h $cm^{-2}$) than that of pristine graphene.[37] The improved performance is benefited from the dominant pyridinic N species and N-doping induced topological defects. Wang *et al.* synthesized N-doped graphene (~2 at%) by thermally annealing GO in $NH_3$, which offers a high reversible capacity of 900 mA h $g^{-1}$ (5 times higher than that of pristine graphene) with an excellent rate performance.[68] Using a similar annealing method, Wu *et al.* prepared B-doped (0.88 at%) and N-doped (3.06 at%) graphene, which gave high reversible capacities of 1549 or 1043 mA h $g^{-1}$ with superior high rate performances, respectively.[59] These B- and N-doped graphene anodes also exhibit excellent energy (~34.9 kW $kg_{electrode}^{-1}$ and ~29.1 kW $kg_{electrode}^{-1}$) and power densities (~320 W h $kg_{electrode}^{-1}$ and ~226 W h $kg_{electrode}^{-1}$), respectively, which are much higher than that of pristine graphene. The improved performance is attributed to the increased conductivity, chemical reactivity, and wettability, resulting from heteroatom doping.

The doping of other heteroatoms (*e.g.* O, Si, P, and S and halogen atoms) has also been reported to enhance the LIB performance. The oxygen groups (*e.g.* carbonyl, ester, carboxylic, epoxide and hydroxyl groups) on GO or rGO can enhance the capacity of LIB *via* Faradaic reaction with Li, for example, $Li^+ + C{=}O + e^- \leftrightarrow C{-}O{-}Li$.[222,223] However, their instability at high current densities compromises the rate performance of LIB.[59] Theoretical calculations show that the binding of Li to B, Si, and P dopants (but not N and S) are energetically favored.[212] Hou *et al.* reported a P-doped graphene (1.32 at%) anode with a higher reversible capacity (~460 mA h $g^{-1}$) than that of pristine graphene.[224] The authors attributed this improved performance to the topological defects caused by P doping.

 

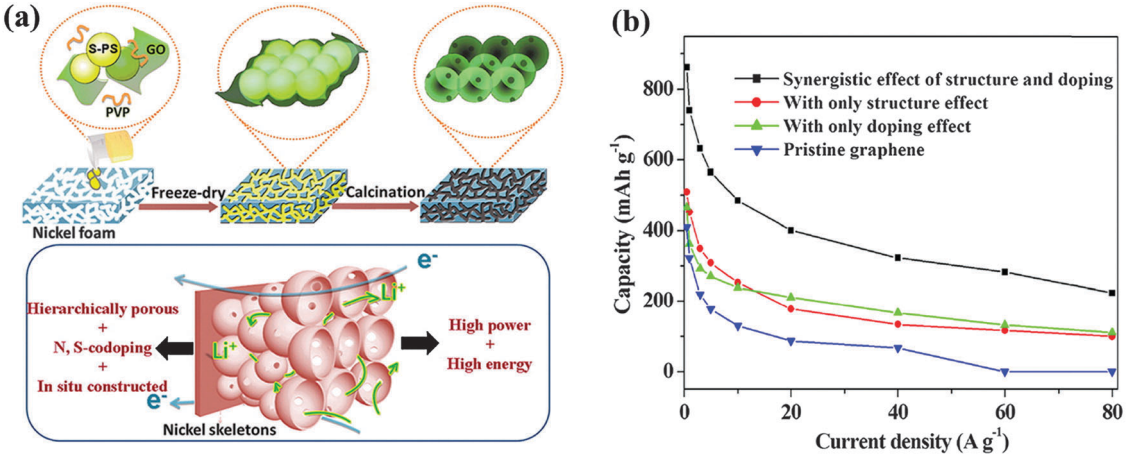


Fig. 19 (a) Schematic illustration of synthesis procedures of 3D N,S co-doped graphene hieratical structure. (b) Comparison of lithium storage performance of pristine graphene and graphene with different effects. Adapted with permission from ref. 225. Copyright (2013) American Chemical Society.

Wang *et al.* fabricated a 3D N,S co-doped graphene hieratical structure (4.2 at% N and 0.94 at% S) as an LIB anode (Fig. 19).[225] Owing to the synergistic effects between the 3D structure and co-dopants, such LIB exhibits an excellent rate performance and a high reversible capacity of 1137 mA h $g^{-1}$, which is ~3 times the theoretical capacity of graphite and much higher than pristine graphene.

Heteroatom doping can be utilized for the anchoring of nanostructured metal oxides (*e.g.* $SnO_2$,[226] MnO,[227] $TiO_2$,[228] $VO_2$,[106] $Zn_2GeO_4$[229] and $\alpha$-$Fe_2O_3$[230]) in order to improve the LIB performance. For example, a sandwich paper of N-doped graphene (8 at%) and $SnO_2$ provides a higher capacity (918 mA h $g^{-1}$) than pure $SnO_2$ nanoparticles or graphene paper.[226] In addition to serving as the conducting network, the intercalated N-doped graphene sheets also prevent the aggregation of $SnO_2$ nanoparticles and provide an elastic buffer space for the volume change of $SnO_2$ nanoparticles during Li-ion insertion/extraction process, which is crucial for high rate performance and cycling stability.

### 4.3 Fuel cells

Developing a state-of-the-art electrocatalyst system with mass-produced and cost-effective materials is pivotal to underpin the industrial operation of fuel cells, in which the sluggish cathodic oxygen reduction reaction (ORR) is often the rate-limiting step. Theoretical and experimental studies have shown that pristine graphene lacks catalytic activities towards ORR and is not efficient in facilitating electron transfer.[231] The deliberate doping of graphene with alien atoms (especially B and N) can transform it to an effective metal-free electrocatalyst for ORR. An electrocatalytic ORR process, depending on the catalyst surface chemistry, often involves complex multiple steps and various adsorbed intermediates. As for the ideal four-electron pathway, oxygen is firstly chemisorbed on the catalyst surface followed by reducing into $OH^-$. B, N and P dopants promote the adsorption of oxygen and O–O bond cleavage because of the charge polarization of the heteroatom–C bond.[232–236] The catalytic ability of S- or Se-doped graphene originates from the creation of spin density due to orbital mismatch between these heteroatoms and C.[53,82] In some cases, a charge polarization and spin density increase may simultaneously contribute (*e.g.*, for N-doped graphene).[41,80,237,238]

The wrinkles and surface tension induced by large-sized dopants also enhance the ORR kinetics by promoting charge transfer.[239,240] The binary doping of impurity atoms into graphene (*e.g.* B–N,[69,201,236] P–N,[201] N–S/Se[45,80,95]) reveals the synergistic effects from different co-dopants on the ORR parameters (*e.g.* onset potential, current density and electron transfer number). A more thorough discussion on B-, N-, P-, S- and Se-doped graphene or other carbon materials for ORR applications can be found in several excellent review articles.[29,241,242]

Halogen-doped graphene for ORR is much less explored albeit its interesting physicochemical and electrical properties. Jeon *et al.* synthesized a series of halogenated graphene nanoplates (XGnPs, X = Cl, Br, or I) by a simple ball milling technique and investigated their electrocatalytic performance towards ORR.[51] Halogen atoms are selectively doped at the edge of GnP with a doping level of 5.89 at% Cl, 2.78 at% Br and 0.95 at% I, respectively. As shown in Fig. 20a, the ORR performance of XGnPs increases in the order of IGnP > BrGnP > ClGnP, which is contrary to the order of the dopant's electronegativity: Cl (3.16) > Br (2.96) > I (2.66). The excellent performance of IGnP (~3.9 electrons) is close to the ideal four-electron process. DFT calculations show that substitution bonding at the zigzag edge (*e.g.* $-Cl^+-$, $-Br^+-$, $-I^+-$) are favorable for $O_2$ adsorption and O–O bond weakening, as evidenced by the increased bond length (Fig. 20c). This is also attributable to the charge transfer between the halogen and $O_2$, the efficiency of which follows the order of Cl < Br < I. In addition to the enhanced catalytic activity, heteroatom doping may also improve the long term stability, selectivity, tolerance to methanol and CO, and electrochemical window (Fig. 20b). Therefore, doped graphene materials are promising to replace the currently used precious metal catalysts (*e.g.*, Pt). Yao *et al.* reported the excellent ORR performance of I-doped graphene synthesized by simple thermal annealing, which exhibited

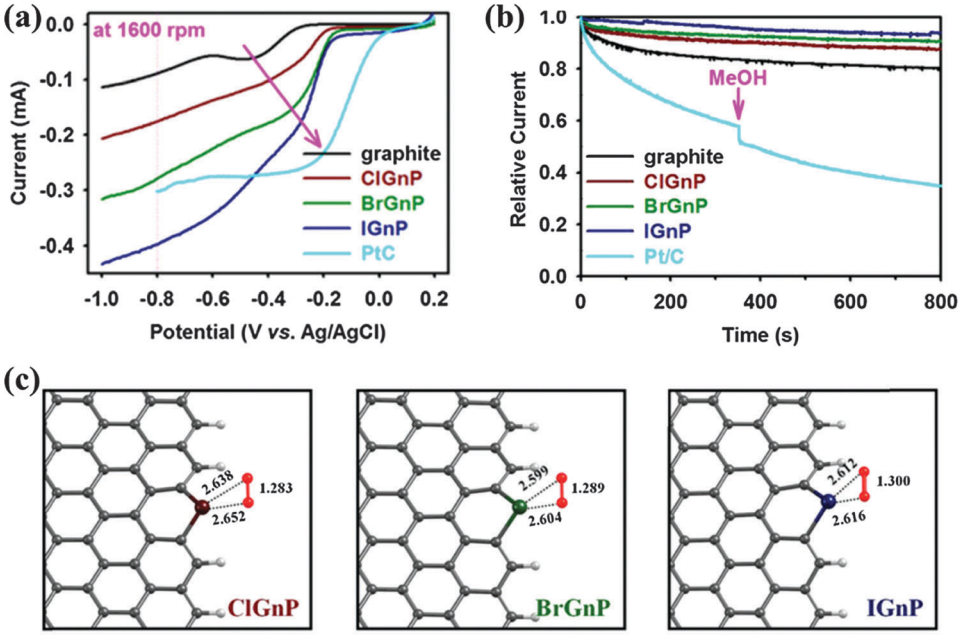


Fig. 20 (a) Linear sweep voltammograms (LSV) at a rotation rate of 1600 rpm and a scan rate of 10 mV $s^{-1}$, showing a gradual increase in current and a positive shift in the onset potential along the order of the pristine graphite, ClGnP, BrGnP, IGnP, and Pt/C (pink arrow). (b) The current–time ($j$–$t$) chronoamperometric responses for ORR for pristine graphite, XGnPs, and commercial Pt/C electrocatalysts in an $O_2$-saturated 0.1 M aq. KOH solution at −0.40 V *vs.* Ag/AgCl and 3.0 M methanol or carbon monoxide (CO, 10 ppm $min^{-1}$) were added at around 360 s. (c) The optimized $O_2$ adsorption geometries onto XGnPs, where halogen covalently linked to two $sp^2$ carbons. The O–O bond length and the shortest C–O bond are shown in angstroms. Adapted with permission from ref. 51. Copyright (2013) Nature Publishing Group.

comparable onset potential, but higher current density as compared with Pt/C electrode.[85] $I_3^-$ induced charge polarization is believed to play a critical role. The ORR performance of doped graphene could be further enhanced by hybridizing it with other catalysts (*e.g.*, $Fe_3O_4$ or $Co_3O_4$[103,243]).

Despite the tremendous progress in the use of doped-graphene materials as a metal-free catalyst, the mechanisms of doping induced ORR enhancement is still not completely understood. In fact, some theoretical and experimental results are contradicting to each other,[65,70,71,74,244–246] resulting from the large heterogeneity in the properties and structures of doped-graphene materials obtained from the current synthesis methods. The possible existence of a trace amount of metal species introduced by the synthesis procedures may also affect the ORR performance and hence, lead to misinterpretation.[58,247,248] The understanding of binary and ternary doped graphene materials is even more challenging.

Doped graphene materials have also been employed as anode materials, especially in direct methanol fuel cells (DMFC). Heteroatom-doped graphene with uniform and dense decoration of precious metal catalysts can improve the catalytic activity and durability of the electrode.[249] Wang *et al.* used S-doped graphene/Pt nanowire composite (S-doped graphene/PtNW) as both the cathode for ORR and anode for methanol oxidation reaction (MOR) (Fig. 21a and b).[81] Towards ORR, it exhibits a higher current density and a lower reduction potential than the state-of-the-art Pt/C catalyst (Fig. 21c). In the case of MOR, the S-doped graphene/PtNW electrode gives ∼3 times higher peak current density in comparison with Pt/C electrode (Fig. 21d). N-doped graphene–CNT hybrid with coated PtRu has also been used as a DMFC anode, which offers a higher (>2 times) power density than the commercial PtRu/C catalyst.[250] N dopants facilitate PtRu immobilization, rendering a better stability in MOR. The outstanding MOR electrocatalytic performance has also been observed for Pt- and PtAu-modified N-doped graphene materials.[251]

### 4.4 Solar cells

**4.4.1 Dye sensitized solar cells (DSSCs).** DSSCs are intensively researched photovoltaic devices to deal with the increasing global energy demand and environmental challenges. The counter electrode in DSSC should be highly catalytic to ensure rapid triiodide reduction and low overpotential. Since oxygen functional groups on graphene can promote the reduction of $I_3^-$ to $I^-$, it has been demonstrated that a DSSC device with a rGO-based counter electrode (with optimized C/O ratio) exhibits a comparable power conversion efficiency (PCE) of 4.99% to that of an expensive Pt counter electrode (5.48%).[252] Xu *et al.* fabricated a counter electrode using a layer-by-layer composition of GO and PDDA (a cationic polymer), followed by electrochemical reduction (ER).[253] DSSC using PDDA@ERGO as the counter electrode and heteroleptic Ru complex C106TBA as the sensitizer reaches a high PCE of 9.5%. The excellent catalytic performance can be attributed to the synergistic effect of oxygen functional groups on ERGO and positively charged N groups in PDDA. Furthermore, such a counter electrode exhibited excellent PCE retention (82% even after 1000 h of light soaking with a full solar intensity of 1000 W $m^{-2}$).

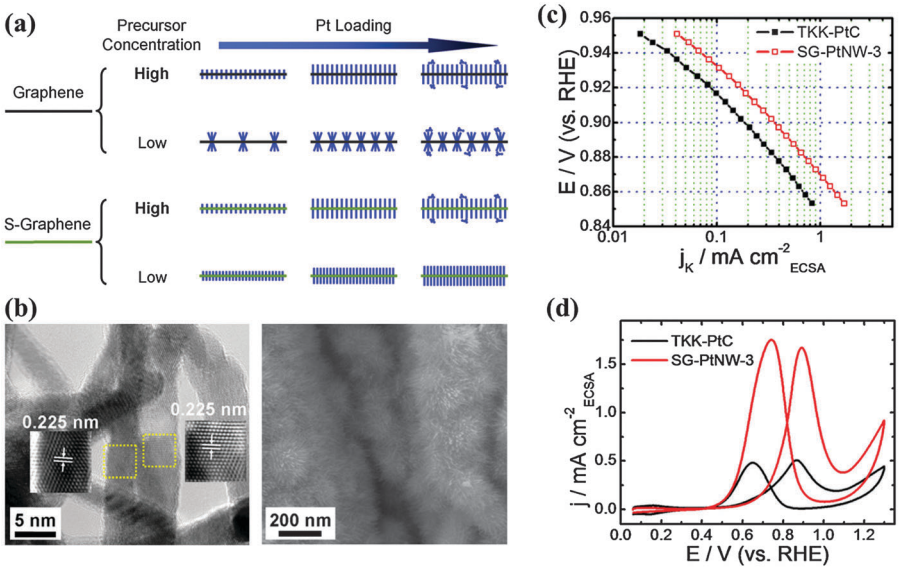


Fig. 21 (a) Schematic illustration of the nanostructural evolution of Pt nanowire arrays grown on graphene and S-doped graphene supports. (b) SEM and high resolution TEM images of S-doped graphene/PtNW catalyst. (c) Specific kinetic current densities ($j_k$) of S-doped graphene/PtNW and Pt/C catalysts for ORR at different potentials. (d) Specific current densities of S-doped graphene/PtNW and Pt/C catalysts toward MOR. Adapted with permission from ref. 81. Copyright (2013) Nature Publishing Group.

A counter electrode with an optimal balance between conductivity and electrocatalytic activity is crucial. B- and N-doped graphene materials are not only highly catalytic to triiodide reduction but also generally more conductive to rGO. Dai *et al.* demonstrated a DSSC equipped with a N-doped graphene (7.6 at%) foam (NGF) counter electrode that offered a PCE of 7.07% as compared to that of a Pt electrode.[254] The NGF electrode exhibited a lower charge transfer resistance ($R_{ct}$ = 5.6 Ω) than that of a Pt electrode (8.8 Ω), indicating its superior catalytic activity towards the $I_3^-/I^-$ redox couple. The high porosity, good hydrophilicity and large surface of NGFs led to a higher short circuit current ($J_{sc}$ = 15.84 mA cm$^{-2}$), open circuit voltage ($V_{oc}$ = 0.77 V) and fill factor (FF = 0.58) than that of rGO foam, N-doped graphene film and rGO film. Cui *et al.* showed that the electrocatalytic activity of N-doped rGO was positively scaled with the doping level.[255] Nitrogen bonding configuration is also important to determine the catalytic properties of N-doped graphene. Compared with pyrrolic N, pyridinic and graphitic N have better catalytic activities and decreased adsorption energy toward $I^-$.[73]

Using a novel redox couple $Co(bpy)_3^{3+/2+}$ and a counter electrode fabricated by electrostatically spraying N-doped graphene nanoplatelets (NGnPs, 2.79 at%) on FTO/glass substrate, Kim *et al.* demonstrated a high-performance DSSC (PCE = 9.05%, $J_{sc}$ = 13.83 mA cm$^{-2}$, FF = 74.2%) superior to the DSSC equipped with a Pt counter electrode (PCE = 8.43%, $J_{sc}$ = 13.48 mA cm$^{-2}$, FF = 70.6%) (Fig. 22).[256] The lower $R_{ct}$ of NGnP electrode (1.73 Ω cm$^{-2}$) than that of the Pt electrode (3.15 Ω cm$^{-2}$) suggests the higher catalytic activity of NGnP. The counter electrode based on NGnPs prepared by the ball milling method also significantly outperforms the Pt electrode.[49] F-doped graphene is also electrocatalytic to $I_3^-/I^-$. Das *et al.* reported the enhanced electrocatalytic activity of graphene towards $I_3^-/I^-$ after $CF_4$-plasma treatment because of the catalytically created active edges, and F-doping enhanced interfacial electron-transfer.[257] It has also been shown that B-doped graphene can serve as the back electrode with the desired ohmic contact to improve the hole-collection ability and photovoltaic efficiency of quantum-dot sensitized solar cells.[57]

**4.4.2 Heterojunction solar cells.** Like Si, heteroatom doping can endow graphene with n- or p-type semiconducting behavior. Hence, doped-graphene materials can be used for p–n junction solar cells. For example, highly transparent B-doped graphene can be used as the p-type electrode in solar cells. Li *et al.* developed a solar cell by interfacing B-doped graphene with n-type Si.[32] Under 1 sun illumination, a $V_{oc}$ of 0.53 V and $J_{sc}$ of 18.8 mA cm$^{-2}$ were obtained, higher than that of pristine graphene/Si solar cell (0.33 V and 15.8 mA cm$^{-2}$). An additional nitric acid fume treatment of B-doped graphene further enhanced the solar cell performance, because additional p-doping by nitric ions increased the electrical conductivity and reduced $R_{ct}$.[258] In a similar mechanism, covalent and ionic Cl doping increases the PCE of a heterojunction solar cell from 5.52% to 8.94%.

Organic solar cells (OSCs) are photovoltaic devices possibly with high flexibility, scalable fabrication process and low manufacturing cost. Bulk heterojunctions (BHJs) produced by the phase-separated blending of electron donors and acceptor materials are most commonly used in OSC devices. Heteroatom-doped graphene sheets can be used to improve conductivity, charge transfer, and thermal and chemical stability of the active layer in BHJ-OSC. Jun *et al.* incorporated N-doped rGO (~8 at%) to the active layer of BHJ-OSC and found a large increase of $J_{sc}$ and PCE in comparison with the device without

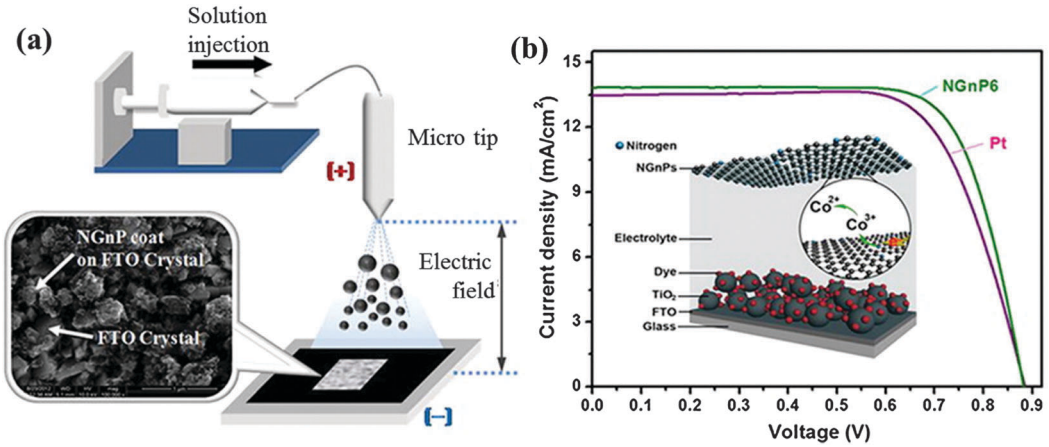


Fig. 22 (a) Schematic representation of an e-spray setup and the SEM image of NGnP coat on FTO crystal. (b) *I–V* characteristics of the DSSCs with Pt and NGnP CEs under one sun illumination (AM 1.5G). Inset is the schematic illustration of DSSC with an NG counter electrode and $Co(bpy)_3^{3+/2+}$ redox reduction on the surface of NGnPs. Adapted with permission from ref. 256. Copyright (2013) American Chemical Society.

graphene additives or with the addition of undoped rGO (Fig. 23a and b).[259] N-doping induces an increase of the work function (~0.4 eV), which, in turn, reduces the $R_{ct}$ value between the active polymer and graphene (Fig. 23c). The maximum PCE of ~4.39% with $J_{sc}$ of ~14.86 mA $cm^{-2}$ was obtained with 0.5 wt% addition of N-doped rGO. Overloading causes the agglomeration of graphene sheets and parasitic paths for current leakage.

### 4.5 Sensors

**4.5.1 Electrochemical sensors.** The performance of electrochemical sensors can be improved by the use of doped graphene materials because the electrochemically active sites introduced by heteroatom doping are able to facilitate charge transfer, adsorption and activation of analytes, and anchoring of functional moieties or molecules (*e.g.*, analyte-specific enzymes). The intrinsic catalytic activity of doped graphene towards the analytes may eliminate the need of recognition elements or mediators (*e.g.*, antibodies or enzymes), rendering the sensors with lower cost and higher stability.

Hydrogen peroxide ($H_2O_2$), which is an important signaling molecule to cells and byproduct of many biological processes, can be directly reduced by heteroatom doped graphene. Shao *et al.* reported an enzyme-free $H_2O_2$ sensor based on N-doped graphene electrode.[260] The sensor exhibited high sensitivity and a wide linear detection range ($10^{-5}$–2.8 mM) because nitrogen-induced charge delocalization weakens the O–O bond of $H_2O_2$ and the electron-donating ability of N-dopants is advantageous for the reduction reaction.

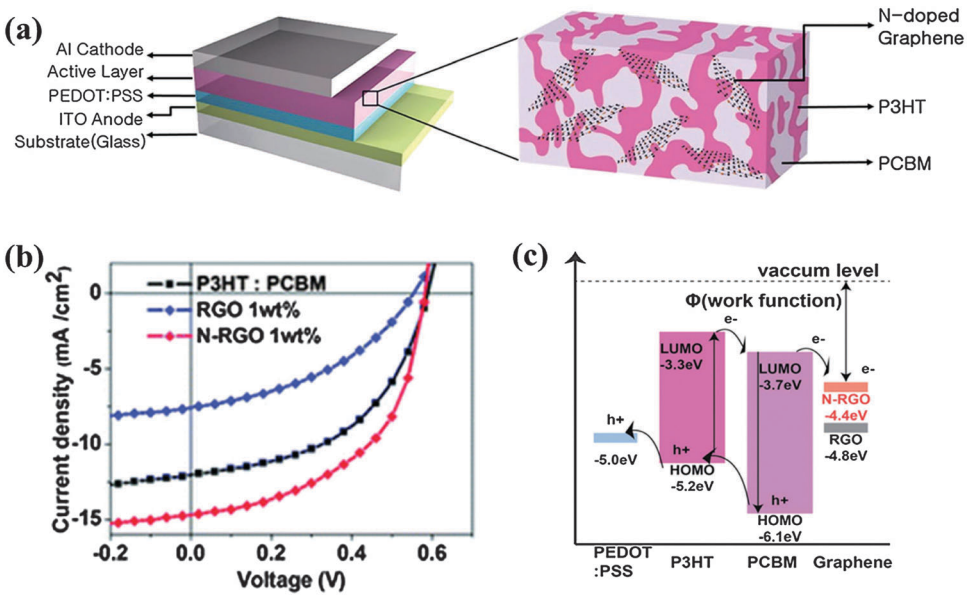


Fig. 23 (a) Schematic of the BHJ solar cell using the N-doped graphene/P3HT: PCBM active layer. (b) *I–V* characteristics of BHJ solar cell devices. (c) Energy-level diagram of a rGO and N-doped RGO/P3HT: PCBM OPV, showing the charge generation and transfer between the two organic components to the electrodes. Adapted with permission from ref. 259. Copyright (2013) Royal Society of Chemistry.

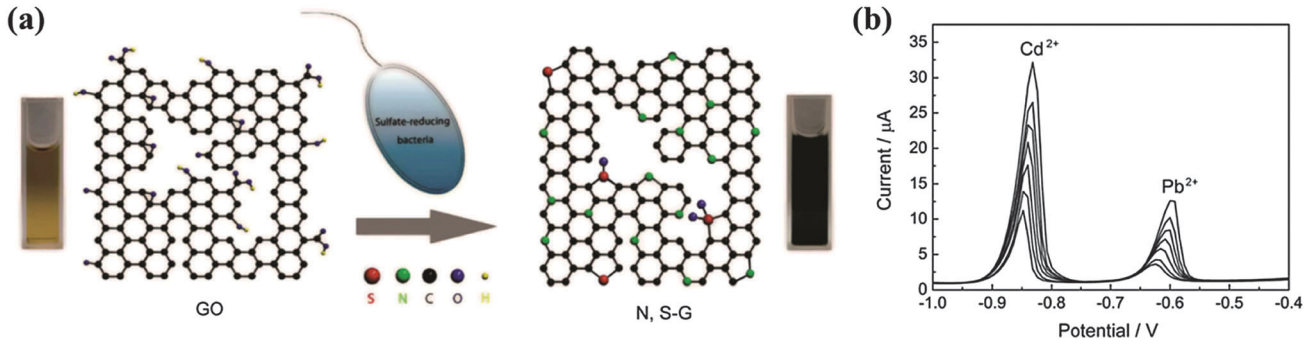


Fig. 24 (a) Schematic illustration of the formation of N,S co-doped graphene by one-pot microbial reduction process. (b) Differential pulse anodic stripping voltammetry of the simultaneous analysis of $Pb^{2+}$and $Cd^{2+}$ with concentrations of 30, 24, 18, 15, 12 and 9 μg $L^{-1}$. Adapted with permission from ref. 266. Copyright (2013) Nature Publishing Group.

A N-doped graphene (4.5 at%) based $H_2O_2$ sensor with a wide linear range (0.5 μM–1.2 mM), low detection limit (0.05 μM), more positive onset reduction potential, and higher reduction current density was developed by Wu *et al.*[87] The improved performance is due to the narrowed (50% reduction) HUMO–LUMO gap (and hence, higher chemical reactivity) after N-doping. Taking the advantages of the high sensitivity and specificity (against interference from other ROS species) of N-doped graphene, the authors also demonstrated the detection of the triggered release of $H_2O_2$ from live cells. Similarly, Yang *et al.* reported a microwave-synthesized B,N co-doped graphene sensor for the highly sensitive detection of $H_2O_2$ and its dynamic release from leukemia cells.[261] The co-doped graphene outperformed (linear range: 0.5 μM to 5 mM; detection limit: 0.05 μM) the graphene sensor with single dopant only (B or N) because the charge polarization induced by B and N co-doping leads to better catalytic activity.

As the enzymatic catalysis of glucose is accompanied by the production of $H_2O_2$, N-doped graphene is also promising for glucose sensing by compositing with glucose oxidase (GOD). Wang *et al.* reported an amperometric sensor based on GOD/N-doped graphene electrode, with a linear detection range of 0.1–1.1 mM and detection limit of 0.01 mM.[262] Owing to the high density of electronic states and active surface chemistry, N-doped graphene facilitates electron transfer from the catalytic center of GOD to the electrode surface.

N-doped graphene prepared by annealing GO with melamine was used to simultaneously and differentially detect ascorbic acid (AA), dopamine (DA) and uric acid (UA) with high sensitivity (detection limits of 2.2 μM, 0.25 μM, and 0.045 μM, respectively).[263] The high sensitivity is ensured by the strong hydrogen bonding and/or π–π interaction between the N-dopants and the target molecules. Li *et al.* found that pyrrolic N is the most reactive to these molecules.[264] N-doped graphene has also been used to electrochemically detect Bisphenol A, a widely used industrial raw material, with a detection limit as low as 5 nM.[265]

Guo *et al.* synthesized N,S co-doped graphene (6.11 at% N dominated by pyridinic N, 1.1 at% S dominated by sulfide bonds) by reducing GO using sulfate-reducing bacteria (Fig. 24).[266] They were able to simultaneously detect $Pb^{2+}$ (detection limit of 0.018 μg $L^{-1}$) and $Cd^{2+}$ (detection limit of 0.016 μg $L^{-1}$), with a linear range of 9–30 μg $L^{-1}$. As compared with single-species doping (N or S alone), N,S co-doping significantly improved the electrocatalytic activity towards $Cd^{2+}$ (> 90%) and $Pb^{2+}$ (>20%) because of the synergistic effects between the dual dopants.

**4.5.2 Electronic sensors.** Graphene materials have been used as sensing elements for the electronic detection of various targets, taking advantage of their high carrier density and mobility, tunable electronic properties of graphene by electrostatic gating or charge transfer, and exposure of all the atoms to the sensing environment.[19,267,268] Heteroatom doping, which can transform graphene from a semimetal to a semiconductor (with p or n-type characteristics), is advantageous for electronic detection based on the field effect.[8] Kwon *et al.* demonstrated a field-effect transistor (FET) based on N-doped graphene for the ultra-sensitive detection of vascular endothelial growth factor (VEGF) with a detection limit as low as 100 fM (Fig. 25).[39] Such N-doped graphene (n-type) was conjugated with anti-VEGF RNA aptamer for the specific recognition of VEGF binding. The binding of positively charged VEGF molecules resulted in the increase of the source-drain current in a concentration dependent manner.

Heteroatom doping can create active sites for the strong adsorption of gas molecules, which, in turn, leads to a dramatic change of graphene conductance. It has been theoretically proven that various electronic sensors can be developed for gas sensing. Zhang *et al.* suggested that B-doped graphene can be used for the sensitive detection of $NO_2$.[269] Dai *et al.* showed that NO and $NO_2$ can be electrically detected by B or S-doped graphene devices.[184] Graphene with metal (*e.g.*, Fe, Co) or Si dopants could be used for $H_2S$ sensing.[270] However, for practical gas sensors, the possible inference from $O_2$ molecules should be considered. It has been found that Si- and P-doped graphene yield the stable chemisorption of $O_2$, whereas B- and N-doped graphene are inert to $O_2$.[271] The strong chemical reactivity of Si-doped graphene with $O_2$ and $NO_2$ was also reported by Zou *et al.*[190]

Despite proven potentials, the experimental demonstrations of doped graphene for gas sensing are rare till now. Using N,Si

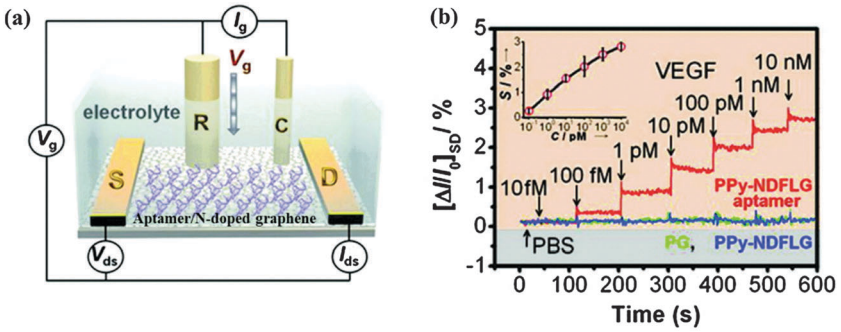


Fig. 25 (a) Schematic diagram of a liquid-ion gated FET using aptamer-conjugated N-doped graphene (Ag/AgCl reference electrode, R; platinum counter electrode, C; source and drain electrodes, S and D). (b) Real-time responses and calibration curve (S in the inset indicates $\Delta I/I_0$) of aptasensor with various vascular endothelial growth factor concentrations. Adapted with permission from ref. 39. Copyright (2012) American Chemical Society.

co-doped graphene for the electrical detection of $NO_2$ was recently presented (Fig. 26a).[272] N,Si co-doped graphene, synthesized by simply annealing GO in the presence of Si-containing IL, shows a resistance decrease while exposed to $NO_2$ gas ($\sim$26% reduction at 21 ppm and 8.8% at 1 ppm) (Fig. 26b). Contradictory to the expectation from the strong chemisorption of $NO_2$ on Si-doped graphene,[190] this sensor shows excellent reversibility. This discrepancy may be explained by the low abundance of Si dopants and the doping configurations different than those assumed in the simulation study.

**4.5.3 Sensors based on surface-enhanced Raman spectroscopy (SERS).** Sensors based on SERS are able to detect the low presence and signature of the analytes utilizing electromagnetic effects induced by precious metal nanoparticles and/or charge transfer effects. It has been shown that the binding of organic molecules on a graphene surface can produce large SERS enhancement, which is attributed to the charge transfer between the target molecules and graphene.[273] The highly polarized heteroatom–C bonds induced by doping may promote the charge transfer between the bound analytes and graphene (hence, improving the SERS signal). As shown by a DFT study, substitutional B-doping can increase the SERS signal of pyridine by 3–4 orders, accompanied with a frequency shift of $\sim$30 $cm^{-1}$.[274] This is attributed to the charge transfer between the negatively charged N atom of pyridine and positively charged B atom of graphene. As for the case of graphitic N doping (however, with a weaker response than B-doped graphene), the SERS enhancement is proposed to originate from the $\pi$ electron transfer from graphene to pyridine.

Lv *et al.* experimentally demonstrated the first SERS sensor based on N-doped graphene.[275] N-doped graphene (0.25 at%, two N atoms separated by one C atom in the same A sublattice as the dominant configuration) synthesized by atmospheric-pressure CVD was used to probe rhodamine B (RhB) molecules (Fig. 27). In comparison with pristine graphene, its N-doped counterpart gave a 10 times stronger signal at 1650 $cm^{-1}$ for the fingerprints of RhB with additional vibration peaks at 1282 $cm^{-1}$, 1531 $cm^{-1}$ and 1567 $cm^{-1}$ (Fig. 27c). The charge transfer (p-doping) by RhB underlies the detection.

### 4.6 Gas storage

Hydrogen is an ideal energy carrier with a non-polluting nature and high energy density. However, its storage is currently a huge technical hurdle for transportation and practical applications. Modifying graphene materials with metal nanoparticles (*e.g.* alkali and alkaline earth metals) can improve the gravimetric storage capacity *via* the polarization-induced interaction between metal and hydrogen atoms.[276] However, decorated nanoparticles suffer from aggregation and poor stability. Heteroatom doping can assist nanoparticle dispersion and high coverage on graphene, as well as $H_2$ adsorption. Parambhath *et al.* synthesized pyrrolic-N dominant graphene (7 at%) for $H_2$ storage.[277] In comparison with undoped graphene, it increased the $H_2$ storage capabilities by 66% (0.88 wt%) at 25 °C and 2 MPa. A further 124% enhancement was achieved with an additional decoration of Pd nanoparticles. The highly dispersed and strongly bonded Pd nanoparticles promote $H_2$ dissociation and the resulting hydrogen atom migration to the

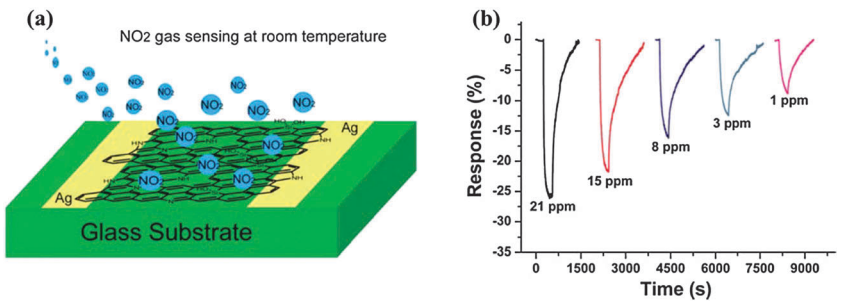


Fig. 26 (a) $NO_2$ sensor based on N,Si co-doped graphene and (b) its response to $NO_2$ for different concentrations. Adapted with permission from ref. 272. Copyright (2013) Royal Society of Chemistry.

 

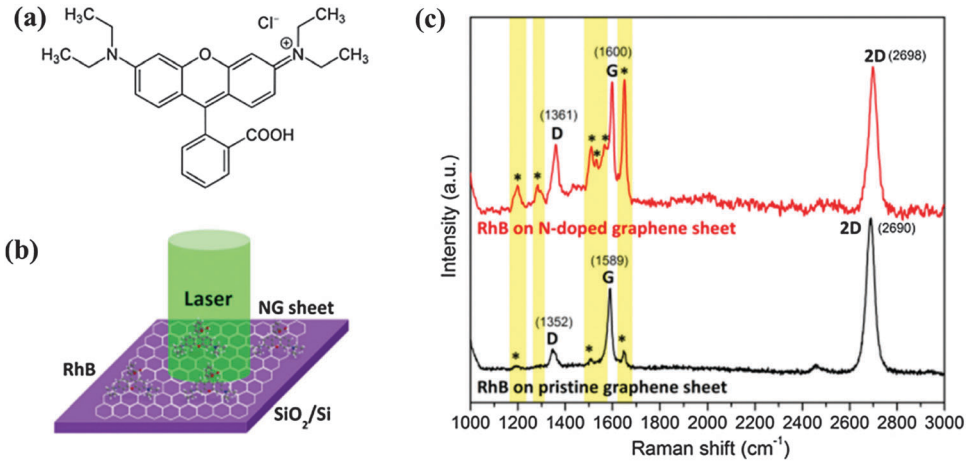


Fig. 27 Enhanced Raman scattering effect of N-doped graphene sheets for probing RhB molecules. (a) Molecular structure of RhB. (b) Schematic illustration of experimental setup. RhB molecules are anchored onto the NG sheet/$SiO_2$/Si substrate. The laser line is 514 nm. (c) Raman signals (*) of RhB molecules. Adapted with permission from ref. 275. Copyright (2012) Nature Publishing Group.

underneath of N-doped graphene. It has been theoretically predicted that $H_2$ absorption on N-doped graphene can be further strengthened by the adsorbed Li atoms.[278,279]

B-doping-induced graphene polarization and electron deficiency is also favorable for hydrogen adsorption, which is even more effective than graphitic-N doping.[118,280] Theoretical calculations show a high $H_2$ storage capacity (8.38 wt%) of Ca-decorated B-doped (12 at%) graphene.[281] Further, the desirable interaction between $H_2$ and B,Ca-decorated graphene makes $H_2$ storage possible even at room temperature and ambient pressure.

Developing techniques to capture greenhouse gases (*e.g.*, $CO_2$) is critical to deal with global warming. Kim *et al.* reported a high gravimetric $CO_2$ storage capacity (2.7 mmol $g^{-1}$ at 298 K and 1 atm) of N-doped graphene, which is comparable to that of PANI-graphene composite at high pressure.[282] The superior performance is attributable to the strong interaction between the N-dopants and $CO_2$ molecules. It is also demonstrated that these N-doped graphene materials possess high recycling stability and selectivity over $N_2$, $CH_4$ and $H_2$. Heteroatom-doped graphene could be used to capture other gases considering its high binding affinity with other gas molecules (*e.g.*, NO, $NO_2$, $SO_2$).[184]

## 5 Summary and perspectives

As discussed in this article, heteroatom doping can endow graphene with various new electromagnetic, physicochemical, optical, and structural properties, depending on the dopants and doping configurations. This greatly extends the arsenal of graphene materials and their potential for a spectrum of applications. Different approaches have been developed for heteroatom doping. Doping type, level and configurations (hence, the properties of obtained materials) are critically determined by the chosen precursors, starting graphene material, reaction time, temperature, *etc.* Despite the tremendous progress made thus far, it is, however, still a current challenge to precisely control heteroatom doping. Based on both experimental and theoretical studies, we have comparably discussed the distinct effects induced by specific dopants, different bonding configurations of a given dopant, and synergistic actions between co-dopants. However, the current understanding on the properties of doped graphene materials is still far from complete and sometimes even contradictory because of the large and uncontrolled heterogeneity of the materials obtained from the current synthesis approaches.

The emerging applications of doped graphene materials for energy storage, energy conversion, sensors, and gas storage have been surveyed in the present study. We envision that a better understanding on the doping mechanisms and doping properties based on both theoretical and experimental investigations, further development of controllable synthesis methods, and incorporation of new dopants will greatly extend the application scope of doped graphene materials. As different dopants, doping configurations and their relative ratios, and compositions of co-dopants confer graphene with distinct properties, the selection and engineering of these parameters should be application-specific. For example, multi-dopants with an optimal balance, which can simultaneously enhance charge polarization, spin density, and conductivity, are desired for ORR.

When graphene transforms from its native 2D structure to 1D (nanoribbons) or 0D (graphene quantum dots. GQD), dramatically altered or new properties arise due to quantum confinement and edge effects. Although not discussed here, we speculate that heteroatom doping on 1D and 0D graphene materials will open up new horizons in graphene research and applications. For example, it has been shown that the fluorescent properties of GQDs can be tailored by heteroatom doping for novel bio-imaging or optical sensing applications.[283–286]

Graphene research will continue to thrive because of the new opportunities provided by heteroatom doping. This article aims to provide useful clues for developing new and controllable synthesis methods and a better understanding of the properties of doped graphene materials. We also hope that it will inspire more exciting applications of this growing family of nanomaterials.

## Acknowledgements

We thank the support from Ministry of Education of Singapore under an AcRF Tier 2 grant (MOE2011-T2-2-010, MOE2012-T2-2-049), the Agency for Science, Technology and Research (A*STAR) under a SERC Grant (102 170 0142), and NNSF of China (61328401).

## References

1 A. K. Geim and K. S. Novoselov, *Nat. Mater.*, 2007, **6**, 183–191.
2 A. H. Castro Neto, F. Guinea, N. M. R. Peres, K. S. Novoselov and A. K. Geim, *Rev. Mod. Phys.*, 2009, **81**, 109–162.
3 D. Jariwala, V. K. Sangwan, L. J. Lauhon, T. J. Marks and M. C. Hersam, *Chem. Soc. Rev.*, 2013, **42**, 2824–2860.
4 K. C. Yung, W. M. Wu, M. P. Pierpoint and F. V. Kusmartsev, *Contemp. Phys.*, 2013, **54**, 233–251.
5 N. Mahmood, C. Z. Zhang, H. Yin and Y. L. Hou, *J. Mater. Chem. A*, 2014, **2**, 15–32.
6 Y. Q. Sun, Q. O. Wu and G. Q. Shi, *Energy Environ. Sci.*, 2011, **4**, 1113–1132.
7 J. Zhang, F. Zhao, Z. P. Zhang, N. Chen and L. T. Qu, *Nanoscale*, 2013, **5**, 3112–3126.
8 Y. X. Liu, X. C. Dong and P. Chen, *Chem. Soc. Rev.*, 2012, **41**, 2283–2307.
9 L. Y. Feng, L. Wu and X. G. Qu, *Adv. Mater.*, 2013, **25**, 168–186.
10 K. Yang, Y. J. Li, X. F. Tan, R. Peng and Z. Liu, *Small*, 2013, **9**, 1492–1503.
11 D. Zhan, J. X. Yan, L. F. Lai, Z. H. Ni, L. Liu and Z. X. Shen, *Adv. Mater.*, 2012, **24**, 4055–4069.
12 W. L. Wei and X. G. Qu, *Small*, 2012, **8**, 2138–2151.
13 Y. W. Zhu, S. Murali, W. W. Cai, X. S. Li, J. W. Suk, J. R. Potts and R. S. Ruoff, *Adv. Mater.*, 2010, **22**, 3906–3924.
14 X. T. Zheng, A. Than, A. Ananthanaraya, D. H. Kim and P. Chen, *ACS Nano*, 2013, **7**, 6278–6286.
15 J. H. Shen, Y. H. Zhu, X. L. Yang and C. Z. Li, *Chem. Commun.*, 2012, **48**, 3686–3699.
16 L. L. Li, G. H. Wu, G. H. Yang, J. Peng, J. W. Zhao and J. J. Zhu, *Nanoscale*, 2013, **5**, 4015–4039.
17 A. Ananthanarayanan, X. W. Wang, P. Routh, B. Sana, S. Lim, D. H. Kim, K. H. Lim, J. Li and P. Chen, *Adv. Funct. Mater.*, 2014, **24**, 3021–3026.
18 S. Dutta and S. K. Pati, *J. Mater. Chem.*, 2010, **20**, 8207–8223.
19 X. Dong, Q. Long, J. Wang, M. B. Chan-Park, Y. Huang, W. Huang and P. Chen, *Nanoscale*, 2011, **3**, 5156–5160.
20 C. Li and G. Q. Shi, *Nanoscale*, 2012, **4**, 5549–5563.
21 X. C. Dong, H. Xu, X. W. Wang, Y. X. Huang, M. B. Chan-Park, H. Zhang, L. H. Wang, W. Huang and P. Chen, *ACS Nano*, 2012, **6**, 3206–3213.
22 Y. C. Yong, X. C. Dong, M. B. Chan-Park, H. Song and P. Chen, *ACS Nano*, 2012, **6**, 2394–2400.
23 X. C. Dong, D. L. Fu, W. J. Fang, Y. M. Shi, P. Chen and L. J. Li, *Small*, 2009, **5**, 1422–1426.
24 X. C. Dong, Q. Long, A. Wei, W. J. Zhang, L. J. Li, P. Chen and W. Huang, *Carbon*, 2012, **50**, 1517–1522.
25 V. Georgakilas, M. Otyepka, A. B. Bourlinos, V. Chandra, N. Kim, K. C. Kemp, P. Hobza, R. Zboril and K. S. Kim, *Chem. Rev.*, 2012, **112**, 6156–6214.
26 R. T. Lv and M. Terrones, *Mater. Lett.*, 2012, **78**, 209–218.
27 U. N. Maiti, W. J. Lee, J. M. Lee, Y. Oh, J. Y. Kim, J. E. Kim, J. Shim, T. H. Han and S. O. Kim, *Adv. Mater.*, 2014, **26**, 40–67.
28 X. K. Kong, C. L. Chen and Q. W. Chen, *Chem. Soc. Rev.*, 2014, **43**, 2841–2857.
29 D. W. Wang and D. S. Su, *Energy Environ. Sci.*, 2014, **7**, 576–591.
30 C. K. Chang, S. Kataria, C. C. Kuo, A. Ganguly, B. Y. Wang, J. Y. Hwang, K. J. Huang, W. H. Yang, S. B. Wang, C. H. Chuang, M. Chen, C. I. Huang, W. F. Pong, K. J. Song, S. J. Chang, J. H. Guo, Y. Tai, M. Tsujimoto, S. Isoda, C. W. Chen, L. C. Chen and K. H. Chen, *ACS Nano*, 2013, **7**, 1333–1341.
31 T. R. Wu, H. L. Shen, L. Sun, B. Cheng, B. Liu and J. C. Shen, *New J. Chem.*, 2012, **36**, 1385–1391.
32 X. Li, L. L. Fan, Z. Li, K. L. Wang, M. L. Zhong, J. Q. Wei, D. H. Wu and H. W. Zhu, *Adv. Energy Mater.*, 2012, **2**, 425–429.
33 L. Ci, L. Song, C. H. Jin, D. Jariwala, D. X. Wu, Y. J. Li, A. Srivastava, Z. F. Wang, K. Storr, L. Balicas, F. Liu and P. M. Ajayan, *Nat. Mater.*, 2010, **9**, 430–435.
34 G. Bepete, D. Voiry, M. Chhowalla, Z. Chiguvare and N. J. Coville, *Nanoscale*, 2013, **5**, 6552–6557.
35 Y. H. Xue, D. S. Yu, L. M. Dai, R. G. Wang, D. Q. Li, A. Roy, F. Lu, H. Chen, Y. Liu and J. Qu, *Phys. Chem. Chem. Phys.*, 2013, **15**, 12220–12226.
36 H. Wang, Y. Zhou, D. Wu, L. Liao, S. L. Zhao, H. L. Peng and Z. F. Liu, *Small*, 2013, **9**, 1316–1320.
37 A. L. M. Reddy, A. Srivastava, S. R. Gowda, H. Gullapalli, M. Dubey and P. M. Ajayan, *ACS Nano*, 2010, **4**, 6337–6342.
38 Z. Jin, J. Yao, C. Kittrell and J. M. Tour, *ACS Nano*, 2011, **5**, 4112–4117.
39 O. S. Kwon, S. J. Park, J. Y. Hong, A. R. Han, J. S. Lee, J. S. Lee, J. H. Oh and J. Jang, *ACS Nano*, 2012, **6**, 1486–1493.
40 Z. Z. Sun, Z. Yan, J. Yao, E. Beitler, Y. Zhu and J. M. Tour, *Nature*, 2010, **468**, 549–552.
41 Y. W. Zhang, J. Ge, L. Wang, D. H. Wang, F. Ding, X. M. Tao and W. Chen, *Sci. Rep.*, 2013, **3**, 2771.
42 D. C. Wei, Y. Q. Liu, Y. Wang, H. L. Zhang, L. P. Huang and G. Yu, *Nano Lett.*, 2009, **9**, 1752–1758.
43 L. T. Qu, Y. Liu, J. B. Baek and L. M. Dai, *ACS Nano*, 2010, **4**, 1321–1326.
44 H. Gao, Z. Liu, L. Song, W. H. Guo, W. Gao, L. J. Ci, A. Rao, W. J. Quan, R. Vajtai and P. M. Ajayan, *Nanotechnology*, 2012, **23**, 275605.
45 J. X. Xu, G. F. Dong, C. H. Jin, M. H. Huang and L. H. Guan, *ChemSusChem*, 2013, **6**, 493–499.

 

46 G. Kalita, K. Wakita, M. Takahashi and M. Umeno, *J. Mater. Chem.*, 2011, **21**, 15209–15213.
47 I. Y. Jeon, Y. R. Shin, G. J. Sohn, H. J. Choi, S. Y. Bae, J. Mahmood, S. M. Jung, J. M. Seo, M. J. Kim, D. W. Chang, L. M. Dai and J. B. Baek, *Proc. Natl. Acad. Sci. U. S. A.*, 2012, **109**, 5588–5593.
48 L. Yan, M. M. Lin, C. Zeng, Z. Chen, S. Zhang, X. M. Zhao, A. G. Wu, Y. P. Wang, L. M. Dai, J. Qu, M. M. Guo and Y. Liu, *J. Mater. Chem.*, 2012, **22**, 8367–8371.
49 I. Y. Jeon, H. J. Choi, M. J. Ju, I. T. Choi, K. Lim, J. Ko, H. K. Kim, J. C. Kim, J. J. Lee, D. Shin, S. M. Jung, J. M. Seo, M. J. Kim, N. Park, L. Dai and J. B. Baek, *Sci. Rep.*, 2013, **3**, 2260.
50 K. Brenner and R. Murali, *Appl. Phys. Lett.*, 2011, **98**, 113115.
51 I. Y. Jeon, H. J. Choi, M. Choi, J. M. Seo, S. M. Jung, M. J. Kim, S. Zhang, L. P. Zhang, Z. H. Xia, L. M. Dai, N. Park and J. B. Baek, *Sci. Rep.*, 2013, **3**, 1810.
52 I. Y. Jeon, H. J. Choi, S. M. Jung, J. M. Seo, M. J. Kim, L. M. Dai and J. B. Baek, *J. Am. Chem. Soc.*, 2013, **135**, 1386–1393.
53 I. Y. Jeon, S. Zhang, L. P. Zhang, H. J. Choi, J. M. Seo, Z. H. Xia, L. M. Dai and J. B. Baek, *Adv. Mater.*, 2013, **25**, 6138–6145.
54 X. J. Lu, J. J. Wu, T. Q. Lin, D. Y. Wan, F. Q. Huang, X. M. Xie and M. H. Jiang, *J. Mater. Chem.*, 2011, **21**, 10685–10689.
55 D. H. Deng, X. L. Pan, L. A. Yu, Y. Cui, Y. P. Jiang, J. Qi, W. X. Li, Q. A. Fu, X. C. Ma, Q. K. Xue, G. Q. Sun and X. H. Bao, *Chem. Mater.*, 2011, **23**, 1188–1193.
56 D. Geng, Y. Hu, Y. Li, R. Li and X. Sun, *Electrochem. Commun.*, 2012, **22**, 65–68.
57 T. Q. Lin, F. Q. Huang, J. Liang and Y. X. Wang, *Energy Environ. Sci.*, 2011, **4**, 862–865.
58 H. L. Peng, Z. Y. Mo, S. J. Liao, H. G. Liang, L. J. Yang, F. Luo, H. Y. Song, Y. L. Zhong and B. Q. Zhang, *Sci. Rep.*, 2013, **3**, 1765.
59 Z. S. Wu, W. C. Ren, L. Xu, F. Li and H. M. Cheng, *ACS Nano*, 2011, **5**, 5463–5471.
60 Z. C. Zuo, Z. Q. Jiang and A. Manthiram, *J. Mater. Chem. A*, 2013, **1**, 13476–13483.
61 X. L. Li, H. L. Wang, J. T. Robinson, H. Sanchez, G. Diankov and H. J. Dai, *J. Am. Chem. Soc.*, 2009, **131**, 15939–15944.
62 L. S. Zhang, X. Q. Liang, W. G. Song and Z. Y. Wu, *Phys. Chem. Chem. Phys.*, 2010, **12**, 12055–12059.
63 G. H. Jun, S. H. Jin, B. Lee, B. H. Kim, W. S. Chae, S. H. Hong and S. Jeon, *Energy Environ. Sci.*, 2013, **6**, 3000–3006.
64 B. Xiong, Y. K. Zhou, Y. Y. Zhao, J. Wang, X. Chen, R. O'Hayre and Z. P. Shao, *Carbon*, 2013, **52**, 181–192.
65 D. S. Geng, Y. Chen, Y. G. Chen, Y. L. Li, R. Y. Li, X. L. Sun, S. Y. Ye and S. Knights, *Energy Environ. Sci.*, 2011, **4**, 760–764.
66 E. Yoo, J. Nakamura and H. S. Zhou, *Energy Environ. Sci.*, 2012, **5**, 6928–6932.
67 T. V. Khai, H. G. Na, D. S. Kwak, Y. J. Kwon, H. Ham, K. B. Shim and H. W. Kim, *J. Mater. Chem.*, 2012, **22**, 17992–18003.
68 H. B. Wang, C. J. Zhang, Z. H. Liu, L. Wang, P. X. Han, H. X. Xu, K. J. Zhang, S. M. Dong, J. H. Yao and G. L. Cui, *J. Mater. Chem.*, 2011, **21**, 5430–5434.
69 S. Y. Wang, L. P. Zhang, Z. H. Xia, A. Roy, D. W. Chang, J. B. Baek and L. M. Dai, *Angew. Chem., Int. Ed.*, 2012, **51**, 4209–4212.
70 L. F. Lai, J. R. Potts, D. Zhan, L. Wang, C. K. Poh, C. H. Tang, H. Gong, Z. X. Shen, L. Y. Jianyi and R. S. Ruoff, *Energy Environ. Sci.*, 2012, **5**, 7936–7942.
71 Z. H. Sheng, L. Shao, J. J. Chen, W. J. Bao, F. B. Wang and X. H. Xia, *ACS Nano*, 2011, **5**, 4350–4358.
72 Z. Y. Lin, G. H. Waller, Y. Liu, M. L. Liu and C. P. Wong, *Carbon*, 2013, **53**, 130–136.
73 S. C. Hou, X. Cai, H. W. Wu, X. Yu, M. Peng, K. Yan and D. C. Zou, *Energy Environ. Sci.*, 2013, **6**, 3356–3362.
74 C. H. Choi, M. W. Chung, S. H. Park and S. I. Woo, *RSC Adv.*, 2013, **3**, 4246–4253.
75 J. Y. Liu, H. Y. Chang, Q. D. Truong and Y. C. Ling, *J. Mater. Chem. C*, 2013, **1**, 1713–1716.
76 R. Li, Z. Wei, X. Gou and W. Xu, *RSC Adv.*, 2013, **3**, 9978–9984.
77 S. B. Yang, L. J. Zhi, K. Tang, X. L. Feng, J. Maier and K. Mullen, *Adv. Funct. Mater.*, 2012, **22**, 3634–3640.
78 H. L. Poh, P. Simek, Z. Sofer and M. Pumera, *ACS Nano*, 2013, **7**, 5262–5272.
79 M. Seredych, J. C. Idrobo and T. J. Bandosz, *J. Mater. Chem. A*, 2013, **1**, 7059–7067.
80 C. H. Choi, M. W. Chung, Y. J. Jun and S. I. Woo, *RSC Adv.*, 2013, **3**, 12417–12422.
81 R. Y. Wang, D. C. Higgins, M. A. Hoque, D. Lee, F. Hassan and Z. W. Chen, *Sci. Rep.*, 2013, **3**, 2431.
82 Z. Yang, Z. Yao, G. F. Li, G. Y. Fang, H. G. Nie, Z. Liu, X. M. Zhou, X. Chen and S. M. Huang, *ACS Nano*, 2012, **6**, 205–211.
83 J. Liang, Y. Jiao, M. Jaroniec and S. Z. Qiao, *Angew. Chem., Int. Ed.*, 2012, **51**, 11496–11500.
84 H. L. Poh, P. Simek, Z. Sofer and M. Pumera, *Chem. – Eur. J.*, 2013, **19**, 2655–2662.
85 Z. Yao, H. G. Nie, Z. Yang, X. M. Zhou, Z. Liu and S. M. Huang, *Chem. Commun.*, 2012, **48**, 1027–1029.
86 P. Wu, Z. W. Cai, Y. Gao, H. Zhang and C. X. Cai, *Chem. Commun.*, 2011, **47**, 11327–11329.
87 P. Wu, Y. D. Qian, P. Du, H. Zhang and C. X. Cai, *J. Mater. Chem.*, 2012, **22**, 6402–6412.
88 Y. H. S. Park, J. O. Hwang, E.-S. Lee, L. B. Casabianca, W. Cai, J. R. Potts, H.-W. Ha, S. Chen, J. Oh, S. O. Kim, Y.-H. Kim, Y. Ishii and R. S. Ruoff, *Nat. Commun.*, 2012, **3**, 1–8.
89 D. H. Long, W. Li, L. C. Ling, J. Miyawaki, I. Mochida and S. H. Yoon, *Langmuir*, 2010, **26**, 16096–16102.
90 B. Jiang, C. Tian, L. Wang, L. Sun, C. Chen, X. Nong, Y. Qiao and H. Fu, *Appl. Surf. Sci.*, 2012, **258**, 3438–3443.
91 L. Sun, L. Wang, C. G. Tian, T. X. Tan, Y. Xie, K. Y. Shi, M. T. Li and H. G. Fu, *RSC Adv.*, 2012, **2**, 4498–4506.

92 J. W. Lee, J. M. Ko and J. D. Kim, *Electrochim. Acta*, 2012, **85**, 459–466.
93 Y. J. Zhang, K. Fugane, T. Mori, L. Niu and J. H. Ye, *J. Mater. Chem.*, 2012, **22**, 6575–6580.
94 Y. Z. Chang, G. Y. Han, J. P. Yuan, D. Y. Fu, F. F. Liu and S. D. A. Li, *J. Power Sources*, 2013, **238**, 492–500.
95 Y. Z. Su, Y. Zhang, X. D. Zhuang, S. Li, D. Q. Wu, F. Zhang and X. L. Feng, *Carbon*, 2013, **62**, 296–301.
96 R. Ballesteros-Garrido, H. G. Baldovi, M. Latorre-Sanchez, M. Alvaro and H. Garcia, *J. Mater. Chem. A*, 2013, **1**, 11728–11734.
97 P. W. Gong, Z. F. Wang, J. Q. Wang, H. G. Wang, Z. P. Li, Z. J. Fan, Y. Xu, X. X. Han and S. R. Yang, *J. Mater. Chem.*, 2012, **22**, 16950–16956.
98 H. X. Chang, J. S. Cheng, X. Q. Liu, J. F. Gao, M. J. Li, J. H. Li, X. M. Tao, F. Ding and Z. J. Zheng, *Chem. – Eur. J.*, 2011, **17**, 8896–8903.
99 J. Zheng, H. T. Liu, B. Wu, C. A. Di, Y. L. Guo, T. Wu, G. Yu, Y. Q. Liu and D. B. Zhu, *Sci. Rep.*, 2012, **2**, 662.
100 H. L. Guo, P. Su, X. F. Kang and S. K. Ning, *J. Mater. Chem. A*, 2013, **1**, 2248–2255.
101 Z. S. Wu, A. Winter, L. Chen, Y. Sun, A. Turchanin, X. L. Feng and K. Mullen, *Adv. Mater.*, 2012, **24**, 5130–5135.
102 Y. Y. Zhao, Y. K. Zhou, B. Xiong, J. Wang, X. Chen, R. O'Hayre and Z. P. Shao, *J. Solid State Electrochem.*, 2013, **17**, 1089–1098.
103 Z. S. Wu, S. B. Yang, Y. Sun, K. Parvez, X. L. Feng and K. Mullen, *J. Am. Chem. Soc.*, 2012, **134**, 9082–9085.
104 S. H. Yang, X. F. Song, P. Zhang and L. Gao, *ACS Appl. Mater. Interfaces*, 2013, **5**, 3317–3322.
105 R. F. Nie, J. J. Shi, W. C. Du, W. S. Ning, Z. Y. Hou and F. S. Xiao, *J. Mater. Chem. A*, 2013, **1**, 9037–9045.
106 C. Nethravathi, C. R. Rajamathi, M. Rajamathi, U. K. Gautam, X. Wang, D. Golberg and Y. Bando, *ACS Appl. Mater. Interfaces*, 2013, **5**, 2708–2714.
107 P. H. Shi, R. J. Su, F. Z. Wan, M. C. Zhu, D. X. Li and S. H. Xu, *Appl. Catal., B*, 2012, **123**, 265–272.
108 H. M. Jeong, J. W. Lee, W. H. Shin, Y. J. Choi, H. J. Shin, J. K. Kang and J. W. Choi, *Nano Lett.*, 2011, **11**, 2472–2477.
109 Y. Wang, Y. Shao, D. W. Matson, J. Li and Y. Lin, *ACS Nano*, 2010, **4**, 1790–1798.
110 S. Gulbagh, D. S. Sutar, V. D. Botcha, K. N. Pavan, S. S. Talwar, R. S. Srinivasa and S. S. Major, *Nanotechnology*, 2013, **24**, 355704.
111 J. Wu, L. M. Xie, Y. G. Li, H. L. Wang, Y. J. Ouyang, J. Guo and H. J. Dai, *J. Am. Chem. Soc.*, 2011, **133**, 19668–19671.
112 X. Zhang, A. Hsu, H. Wang, Y. Song, J. Kong, M. S. Dresselhaus and T. Palacios, *ACS Nano*, 2013, **7**, 7262–7270.
113 B. Li, L. Zhou, D. Wu, H. L. Peng, K. Yan, Y. Zhou and Z. F. Liu, *ACS Nano*, 2011, **5**, 5957–5961.
114 N. Li, Z. Y. Wang, K. K. Zhao, Z. J. Shi, Z. N. Gu and S. K. Xu, *Carbon*, 2010, **48**, 255–259.
115 L. S. Panchakarla, K. S. Subrahmanyam, S. K. Saha, A. Govindaraj, H. R. Krishnamurthy, U. V. Waghmare and C. N. R. Rao, *Adv. Mater.*, 2009, **21**, 4726–4730.
116 B. S. Shen, J. T. Chen, X. B. Yan and Q. J. Xue, *RSC Adv.*, 2012, **2**, 6761–6764.
117 P. Rani and V. K. Jindal, *RSC Adv.*, 2013, **3**, 802–812.
118 R. H. Miwa, T. B. Martins and A. Fazzio, *Nanotechnology*, 2008, **19**, 155708.
119 R. Faccio, L. Fernandez-Werner, H. Pardo, C. Goyenola, O. N. Ventura and A. W. Mombru, *J. Phys. Chem. C*, 2010, **114**, 18961–18971.
120 K. Z.M. Magdalena Woínska and J.-A. Majewski, *Phys. Status Solidi C*, 2013, **10**, 1167–1171.
121 L. S. Panchokarla, K. S. Subrahmanyam, S. K. Saha, A. Govindaraj, H. R. Krishnamurthy, U. V. Waghmare and C. N. R. Rao, *Adv. Mater.*, 2009, **21**, 4726–4730.
122 B. Mortazavi and S. Ahzi, *Solid State Commun.*, 2012, **152**, 1503–1507.
123 B. Zheng, P. Hermet and L. Henrard, *ACS Nano*, 2010, **4**, 4165–4173.
124 Q. Q. Zhu, J. H. Yu, W. S. Zhang, H. Z. Dong and L. F. Dong, *J. Renewable Sustainable Energy*, 2013, **5**, 021408.
125 S. Mukherjee and T. P. Kaloni, *J. Nanopart. Res.*, 2012, **14**, 1059.
126 A. Lherbier, X. Blase, Y. M. Niquet, F. Triozon and S. Roche, *Phys. Rev. Lett.*, 2008, **101**, 036808.
127 H. Mousavi and R. Moradian, *Solid State Sci.*, 2011, **13**, 1459–1464.
128 S. O. Guillaume, B. Zheng, J. C. Charlier and L. Henrard, *Phys. Rev. B: Condens. Matter Mater. Phys.*, 2012, **85**, 035444.
129 D. Usachov, O. Vilkov, A. Gruneis, D. Haberer, A. Fedorov, V. K. Adamchuk, A. B. Preobrajenski, P. Dudin, A. Barinov, M. Oehzelt, C. Laubschat and D. V. Vyalikh, *Nano Lett.*, 2011, **11**, 5401–5407.
130 M. M. Yang, L. Zhou, J. Y. Wang, Z. F. Liu and Z. R. Liu, *J. Phys. Chem. C*, 2012, **116**, 844–850.
131 Z. F. Hou, X. L. Wang, T. Ikeda, K. Terakura, M. Oshima and M. Kakimoto, *Phys. Rev. B: Condens. Matter Mater. Phys.*, 2013, **87**, 165401.
132 Z. F. Hou, X. L. Wang, T. Ikeda, K. Terakura, M. Oshima, M. Kakimoto and S. Miyata, *Phys. Rev. B: Condens. Matter Mater. Phys.*, 2012, **85**, 165439.
133 P. Wu, P. Du, H. Zhang and C. Cai, *Phys. Chem. Chem. Phys.*, 2013, **15**, 6920–6928.
134 A. Lherbier, A. R. Botello-Mendez and J. C. Charlier, *Nano Lett.*, 2013, **13**, 1446–1450.
135 D. Wei, Y. Liu, Y. Wang, H. Zhang, L. Huang and G. Yu, *Nano Lett.*, 2009, **9**, 1752–1758.
136 S. Jalili and R. Vaziri, *Mol. Phys.*, 2011, **109**, 687–694.
137 T. Schiros, D. Nordlund, L. Palova, D. Prezzi, L. Y. Zhao, K. S. Kim, U. Wurstbauer, C. Gutierrez, D. Delongchamp, C. Jaye, D. Fischer, H. Ogasawara, L. G. M. Pettersson, D. R. Reichman, P. Kim, M. S. Hybertsen and A. N. Pasupathy, *Nano Lett.*, 2012, **12**, 4025–4031.
138 Y. F. Lu, S. T. Lo, J. C. Lin, W. J. Zhang, J. Y. Lu, F. H. Liu, C. M. Tseng, Y. H. Lee, C. T. Liang and L. J. Li, *ACS Nano*, 2013, **7**, 6522–6532.
139 F. Cervantes-Sodi, G. Csanyi, S. Piscanec and A. C. Ferrari, *Phys. Rev. B: Condens. Matter Mater. Phys.*, 2008, **77**, 165427.

 

140 E. Velez-Fort, C. Mathieu, E. Pallecchi, M. Pigneur, M. G. Silly, R. Belkhou, M. Marangolo, A. Shukla, F. Sirotti and A. Ouerghi, *ACS Nano*, 2012, **6**, 10893–10900.
141 J. O. Hwang, J. S. Park, D. S. Choi, J. Y. Kim, S. H. Lee, K. E. Lee, Y. H. Kim, M. H. Song, S. Yoo and S. O. Kim, *ACS Nano*, 2012, **6**, 159–167.
142 Z. Luo, S. Lim, Z. Tian, J. Shang, L. Lai, B. MacDonald, C. Fu, Z. Shen, T. Yu and J. Lin, *J. Mater. Chem.*, 2011, **21**, 8038–8044.
143 Y. Liu, Q. Feng, N. J. Tang, X. G. Wan, F. C. Liu, L. Y. Lv and Y. W. Du, *Carbon*, 2013, **60**, 549–551.
144 Y. Li, Z. Zhou, P. Shen and Z. Chen, *ACS Nano*, 2009, **3**, 1952–1958.
145 J. W. Chiou, S. C. Ray, S. I. Peng, C. H. Chuang, B. Y. Wang, H. M. Tsai, C. W. Pao, H. J. Lin, Y. C. Shao, Y. F. Wang, S. C. Chen, W. F. Pong, Y. C. Yeh, C. W. Chen, L. C. Chen, K. H. Chen, M. H. Tsai, A. Kumar, A. Ganguly, P. Papakonstantinou, H. Yamane, N. Kosugi, T. Regier, L. Liu and T. K. Sham, *J. Phys. Chem. C*, 2012, **116**, 16251–16258.
146 T. Van Khai, H. G. Na, D. S. Kwak, Y. J. Kwon, H. Ham, K. B. Shim and H. W. Kim, *J. Mater. Chem.*, 2012, **22**, 17992–18003.
147 M. Li, Z. Wu, W. Ren, H. Cheng, N. Tang, W. Wu, W. Zhong and Y. Du, *Carbon*, 2012, **50**, 5286–5291.
148 H.-m. Wang, H.-x. Wang, Y. Chen, Y.-j. Liu, J.-x. Zhao, Q.-h. Cai and X.-z. Wang, *Appl. Surf. Sci.*, 2013, **273**, 302–309.
149 Z.-W. Liu, F. Peng, H.-J. Wang, H. Yu, W.-X. Zheng and J. Yang, *Angew. Chem., Int. Ed.*, 2011, **50**, 3257–3261.
150 T. Schiros, D. Nordlund, L. Palova, D. Prezzi, L. Y. Zhao, K. S. Kim, U. Wurstbauer, C. Gutierrez, D. Delongchamp, C. Jaye, D. Fischer, H. Ogasawara, L. G. M. Pettersson, D. R. Reichman, P. Kim, M. S. Hybertsen and A. N. Pasupathy, *Nano Lett.*, 2012, **12**, 4025–4031.
151 S. Some, J. Kim, K. Lee, A. Kulkarni, Y. Yoon, S. Lee, T. Kim and H. Lee, *Adv. Mater.*, 2012, **24**, 5481–5486.
152 P. A. Denis, *Comput. Mater. Sci.*, 2013, **67**, 203–206.
153 J. Y. Dai and J. M. Yuan, *J. Phys.: Condens. Matter*, 2010, **22**, 225501.
154 K. A. Mkhoyan, A. W. Contryman, J. Silcox, D. A. Stewart, G. Eda, C. Mattevi, S. Miller and M. Chhowalla, *Nano Lett.*, 2009, **9**, 1058–1063.
155 D. W. Boukhvalov and M. I. Katsnelson, *J. Am. Chem. Soc.*, 2008, **130**, 10697–10701.
156 T. Szabo, O. Berkesi, P. Forgo, K. Josepovits, Y. Sanakis, D. Petridis and I. Dekany, *Chem. Mater.*, 2006, **18**, 2740–2749.
157 I. Jung, D. A. Dikin, R. D. Piner and R. S. Ruoff, *Nano Lett.*, 2008, **8**, 4283–4287.
158 Z. Xu, Y. Bando, L. Liu, W. L. Wang, X. D. Bai and D. Golberg, *ACS Nano*, 2011, **5**, 4401–4406.
159 S. Kim, S. Zhou, Y. K. Hu, M. Acik, Y. J. Chabal, C. Berger, W. de Heer, A. Bongiorno and E. Riedo, *Nat. Mater.*, 2012, **11**, 544–549.
160 P. V. Kumar, M. Bernardi and J. C. Grossman, *ACS Nano*, 2013, **7**, 1638–1645.
161 H. P. Jia, D. R. Dreyer and C. W. Bielawski, *Tetrahedron*, 2011, **67**, 4431–4434.
162 D. S. Su, J. Zhang, B. Frank, A. Thomas, X. C. Wang, J. Paraknowitsch and R. Schlogl, *ChemSusChem*, 2010, **3**, 169–180.
163 D. R. Dreyer, H. P. Jia and C. W. Bielawski, *Angew. Chem., Int. Ed.*, 2010, **49**, 6813–6816.
164 D. R. Dreyer, S. Park, C. W. Bielawski and R. S. Ruoff, *Chem. Soc. Rev.*, 2010, **39**, 228–240.
165 C. L. Su and K. P. Loh, *Acc. Chem. Res.*, 2013, **46**, 2275–2285.
166 P. A. Denis, *Chem. Phys. Lett.*, 2010, **492**, 251–257.
167 P. A. Denis, R. Faccio and A. W. Mombru, *ChemPhysChem*, 2009, **10**, 715–722.
168 S. Glenis, A. J. Nelson and M. M. Labes, *J. Appl. Phys.*, 1999, **86**, 4464–4466.
169 R. Zboril, F. Karlicky, A. B. Bourlinos, T. A. Steriotis, A. K. Stubos, V. Georgakilas, K. Safarova, D. Jancik, C. Trapalis and M. Otyepka, *Small*, 2010, **6**, 2885–2891.
170 M. A. Ribas, A. K. Singh, P. B. Sorokin and B. I. Yakobson, *Nano Res.*, 2011, **4**, 143–152.
171 J. T. Robinson, J. S. Burgess, C. E. Junkermeier, S. C. Badescu, T. L. Reinecke, F. K. Perkins, M. K. Zalalutdniov, J. W. Baldwin, J. C. Culbertson, P. E. Sheehan and E. S. Snow, *Nano Lett.*, 2010, **10**, 3001–3005.
172 R. R. Nair, W. C. Ren, R. Jalil, I. Riaz, V. G. Kravets, L. Britnell, P. Blake, F. Schedin, A. S. Mayorov, S. J. Yuan, M. I. Katsnelson, H. M. Cheng, W. Strupinski, L. G. Bulusheva, A. V. Okotrub, I. V. Grigorieva, A. N. Grigorenko, K. S. Novoselov and A. K. Geim, *Small*, 2010, **6**, 2877–2884.
173 K. J. Jeon, Z. Lee, E. Pollak, L. Moreschini, A. Bostwick, C. M. Park, R. Mendelsberg, V. Radmilovic, R. Kostecki, T. J. Richardson and E. Rotenberg, *ACS Nano*, 2011, **5**, 1042–1046.
174 P. V. C. Medeiros, A. J. S. Mascarenhas, F. D. Mota and C. M. C. de Castilho, *Nanotechnology*, 2010, **21**, 485701.
175 M. Klintenberg, S. Lebegue, M. I. Katsnelson and O. Eriksson, *Phys. Rev. B: Condens. Matter Mater. Phys.*, 2010, **81**, 085433.
176 H. Sahin and S. Ciraci, *J. Phys. Chem. C*, 2012, **116**, 24075–24083.
177 A. Yaya, C. P. Ewels, I. Suarez-Martinez, P. Wagner, S. Lefrant, A. Okotrub, L. Bulusheva and P. R. Briddon, *Phys. Rev. B: Condens. Matter Mater. Phys.*, 2011, **83**, 045411.
178 R. Balog, B. Jorgensen, L. Nilsson, M. Andersen, E. Rienks, M. Bianchi, M. Fanetti, E. Laegsgaard, A. Baraldi, S. Lizzit, Z. Sljivancanin, F. Besenbacher, B. Hammer, T. G. Pedersen, P. Hofmann and L. Hornekaer, *Nat. Mater.*, 2010, **9**, 315–319.
179 D. C. Elias, R. R. Nair, T. M. G. Mohiuddin, S. V. Morozov, P. Blake, M. P. Halsall, A. C. Ferrari, D. W. Boukhvalov, M. I. Katsnelson, A. K. Geim and K. S. Novoselov, *Science*, 2009, **323**, 610–613.

180 M. Pumera and C. H. A. Wong, *Chem. Soc. Rev.*, 2013, **42**, 5987–5995.
181 S. C. Ray, N. Soin, T. Makgato, C. H. Chuang, W. F. Pong, S. S. Roy, S. K. Ghosh, A. M. Strydom and J. A. McLaughlin, *Sci. Rep.*, 2014, **4**, 3862.
182 R. Jayasingha, A. Sherehiy, S. Y. Wu and G. U. Sumanasekera, *Nano Lett.*, 2013, **13**, 5098–5105.
183 Y. Lee, S. Lee, Y. Hwang and Y. C. Chung, *Appl. Surf. Sci.*, 2014, **289**, 445–449.
184 J. Y. Dai, J. M. Yuan and P. Giannozzi, *Appl. Phys. Lett.*, 2009, **95**, 232105.
185 Z. M. Ao, J. Yang, S. Li and Q. Jiang, *Chem. Phys. Lett.*, 2008, **461**, 276–279.
186 J. X. Zhao, Y. Chen and H. G. Fu, *Theor. Chem. Acc.*, 2012, **131**, 1242.
187 Y. Chen, X. C. Yang, Y. J. Liu, J. X. Zhao, Q. H. Cai and X. Z. Wang, *J. Mol. Graphics Modell.*, 2013, **39**, 126–132.
188 Y. Chen, Y. J. Liu, H. X. Wang, J. X. Zhao, Q. H. Cai, X. Z. Wang and Y. H. Ding, *ACS Appl. Mater. Interfaces*, 2013, **5**, 5994–6000.
189 Y. Chen, B. Gao, J. X. Zhao, Q. H. Cai and H. G. Fu, *J. Mol. Model.*, 2012, **18**, 2043–2054.
190 Y. Zou, F. Li, Z. H. Zhu, M. W. Zhao, X. G. Xu and X. Y. Su, *Eur. Phys. J. B*, 2011, **81**, 475–479.
191 H. Nozaki and S. Itoh, *J. Phys. Chem. Solids*, 1996, **57**, 41–49.
192 B. Sumanta and S. Biplab, Graphene-Boron Nitride Composite: A Material with Advanced Functionalities, in *Composites and Their Properties*, ed. N. Hu, InTech, 2012, ch. 1, ISBN 978-953-51-07, http://www.intechopen.com/books/composites-and-their-properties/graphene-boron-nitride-composite-a-material-with-advanced-functionalities.
193 P. Rani and V. K. Jindal, *Appl. Nanosci.*, 2013, 1–8.
194 B. Muchharla, A. Pathak, Z. Liu, L. Song, T. Jayasekera, S. Kar, R. Vajtai, L. Balicas, P. M. Ajayan, S. Talapatra and N. Ali, *Nano Lett.*, 2013, **13**, 3476–3481.
195 H. Tachikawa, T. Iyama and K. Azumi, *Jpn. J. Appl. Phys.*, 2011, **50**, 01BJ03.
196 M. O. Watanabe, S. Itoh, K. Mizushima and T. Sasaki, *J. Appl. Phys.*, 1995, **78**, 2880–2882.
197 M. O. Watanabe, S. Itoh, T. Sasaki and K. Mizushima, *Phys. Rev. Lett.*, 1996, **77**, 187–189.
198 B. Muchharla, A. Pathak, Z. Liu, L. Song, T. Jayasekera, S. Kar, R. Vajtai, L. Balicas, P. M. Ajayan, S. Talapatra and N. Ali, *Nano Lett.*, 2013, **13**, 3476–3481.
199 X. F. Fan, Z. X. Shen, A. Q. Liu and J. L. Kuo, *Nanoscale*, 2012, **4**, 2157–2165.
200 X. H. Deng, Y. Q. Wu, J. Y. Dai, D. D. Kang and D. Y. Zhang, *Phys. Lett. A*, 2011, **375**, 3890–3894.
201 C. H. Choi, M. W. Chung, H. C. Kwon, S. H. Park and S. I. Woo, *J. Mater. Chem. A*, 2013, **1**, 3694–3699.
202 T. Kwon, H. Nishihara, H. Itoi, Q. H. Yang and T. Kyotani, *Langmuir*, 2009, **25**, 11961–11968.
203 B. Xu, S. F. Yue, Z. Y. Sui, X. T. Zhang, S. S. Hou, G. P. Cao and Y. S. Yang, *Energy Environ. Sci.*, 2011, **4**, 2826–2830.
204 V. H. Pham, S. H. Hur, E. J. Kim, B. S. Kim and J. S. Chung, *Chem. Commun.*, 2013, **49**, 6665–6667.
205 L. Sun, L. Wang, C. Tian, T. Tan, Y. Xie, K. Shi, M. Li and H. Fu, *RSC Adv.*, 2012, **2**, 4498–4506.
206 W. Fan, Y.-Y. Xia, W. W. Tjiu, P. K. Pallathadka, C. He and T. Liu, *J. Power Sources*, 2013, **243**, 973–981.
207 P. Karthika, N. Rajalakshmi and K. S. Dhathathreyan, *J. Nanosci. Nanotechnol.*, 2013, **13**, 1746–1751.
208 G. Hasegawa, M. Aoki, K. Kanamori, K. Nakanishi, T. Hanada and K. Tadanaga, *J. Mater. Chem.*, 2011, **21**, 2060–2063.
209 X. C. Zhao, Q. Zhang, C. M. Chen, B. S. Zhang, S. Reiche, A. Q. Wang, T. Zhang, R. Schlogl and D. S. Su, *Nano Energy*, 2012, **1**, 624–630.
210 H. B. Wang, T. Maiyalagan and X. Wang, *ACS Catal.*, 2012, **2**, 781–794.
211 S. Yang, X. Song, P. Zhang and L. Gao, *ACS Appl. Mater. Interfaces*, 2013, **5**, 3317–3322.
212 Y. Y. Liu, V. I. Artyukhov, M. J. Liu, A. R. Harutyunyan and B. I. Yakobson, *J. Phys. Chem. Lett.*, 2013, **4**, 1737–1742.
213 D. Das, S. Kim, K. R. Lee and A. K. Singh, *Phys. Chem. Chem. Phys.*, 2013, **15**, 15128–15134.
214 D. Y. Pan, S. Wang, B. Zhao, M. H. Wu, H. J. Zhang, Y. Wang and Z. Jiao, *Chem. Mater.*, 2009, **21**, 3136–3142.
215 F. Yao, F. Gunes, H. Q. Ta, S. M. Lee, S. J. Chae, K. Y. Sheem, C. S. Cojocaru, S. S. Xie and Y. H. Lee, *J. Am. Chem. Soc.*, 2012, **134**, 8646–8654.
216 C. Ma, X. Shao and D. Cao, *J. Mater. Chem.*, 2012, **22**, 8911–8915.
217 D. H. Wu, Y. F. Li and Z. Zhou, *Theor. Chem. Acc.*, 2011, **130**, 209–213.
218 X. L. Wang, Z. Zeng, H. Ahn and G. X. Wang, *Appl. Phys. Lett.*, 2009, **95**, 183103.
219 S. H. Gao, Z. Y. Ren, L. J. Wan, J. M. Zheng, P. Guo and Y. X. Zhou, *Appl. Surf. Sci.*, 2011, **257**, 7443–7446.
220 Y. X. Yu, *Phys. Chem. Chem. Phys.*, 2013, **15**, 16819–16827.
221 X. K. Kong and Q. W. Chen, *Phys. Chem. Chem. Phys.*, 2013, **15**, 12982–12987.
222 S. W. Lee, N. Yabuuchi, B. M. Gallant, S. Chen, B. S. Kim, P. T. Hammond and Y. Shao-Horn, *Nat. Nanotechnol.*, 2010, **5**, 531–537.
223 S. W. Lee, B. S. Kim, S. Chen, Y. Shao-Horn and P. T. Hammond, *J. Am. Chem. Soc.*, 2009, **131**, 671–679.
224 C. Z. Zhang, N. Mahmood, H. Yin, F. Liu and Y. L. Hou, *Adv. Mater.*, 2013, **25**, 4932–4937.
225 Z. L. Wang, D. Xu, H. G. Wang, Z. Wu and X. B. Zhang, *ACS Nano*, 2013, **7**, 2422–2430.
226 X. Wang, X. Q. Cao, L. Bourgeois, H. Guan, S. M. Chen, Y. T. Zhong, D. M. Tang, H. Q. Li, T. Y. Zhai, L. Li, Y. Bando and D. Golberg, *Adv. Funct. Mater.*, 2012, **22**, 2682–2690.
227 K. Zhang, P. Han, L. Gu, L. Zhang, Z. Liu, Q. Kong, C. Zhang, S. Dong, Z. Zhang, J. Yao, H. Xu, G. Cui and L. Chen, *ACS Appl. Mater. Interfaces*, 2012, **4**, 658–664.
228 D. Li, D. Q. Shi, Z. W. Liu, H. K. Liu and Z. P. Guo, *J. Nanopart. Res.*, 2013, **15**, 1674.

229 F. Zou, X. L. Hu, Y. M. Sun, W. Luo, F. F. Xia, L. Qie, Y. Jiang and Y. H. Huang, *Chem. – Eur. J.*, 2013, **19**, 6027–6033.
230 X. Wang, W. Tian, D. Liu, C. Zhi, Y. Bando and D. Golberg, *Nano Energy*, 2013, **2**, 257–267.
231 D. A. C. Brownson, L. J. Munro, D. K. Kampouris and C. E. Banks, *RSC Adv.*, 2011, **1**, 978–988.
232 Z. H. Sheng, H. L. Gao, W. J. Bao, F. B. Wang and X. H. Xia, *J. Mater. Chem.*, 2012, **22**, 390–395.
233 X. G. Bao, X. W. Nie, D. von Deak, E. Biddinger, W. J. Luo, A. Asthagiri, U. Ozkan and C. Hadad, *Top. Catal.*, 2013, **56**, 1623–1633.
234 R. Li, Z. D. Wei, X. L. Gou and W. Xu, *RSC Adv.*, 2013, **3**, 9978–9984.
235 X. F. Fan, W. T. Zheng and J. L. Kuo, *RSC Adv.*, 2013, **3**, 5498–5505.
236 Y. Zheng, Y. Jiao, L. Ge, M. Jaroniec and S. Z. Qiao, *Angew. Chem., Int. Ed.*, 2013, **52**, 3110–3116.
237 X. K. Kong, Q. W. Chen and Z. Y. Sun, *ChemPhysChem*, 2013, **14**, 514–519.
238 L. P. Zhang and Z. H. Xia, *J. Phys. Chem. C*, 2011, **115**, 11170–11176.
239 Z. P. Jin, H. G. Nie, Z. Yang, J. Zhang, Z. Liu, X. J. Xu and S. M. Huang, *Nanoscale*, 2012, **4**, 6455–6460.
240 A. G. Garcia, S. E. Baltazar, A. H. R. Castro, J. F. P. Robles and A. Rubio, *J. Comput. Theor. Nanosci.*, 2008, **5**, 2221–2229.
241 C. Z. Zhu and S. J. Dong, *Nanoscale*, 2013, **5**, 1753–1767.
242 Z. Yang, H. G. Nie, X. Chen, X. H. Chen and S. M. Huang, *J. Power Sources*, 2013, **236**, 238–249.
243 Y. Y. Liang, Y. G. Li, H. L. Wang, J. G. Zhou, J. Wang, T. Regier and H. J. Dai, *Nat. Mater.*, 2011, **10**, 780–786.
244 Z. Q. Luo, S. H. Lim, Z. Q. Tian, J. Z. Shang, L. F. Lai, B. MacDonald, C. Fu, Z. X. Shen, T. Yu and J. Y. Lin, *J. Mater. Chem.*, 2011, **21**, 8038–8044.
245 H. Kim, K. Lee, S. I. Woo and Y. Jung, *Phys. Chem. Chem. Phys.*, 2011, **13**, 17505–17510.
246 K. R. Lee, K. U. Lee, J. W. Lee, B. T. Ahn and S. I. Woo, *Electrochem. Commun.*, 2010, **12**, 1052–1055.
247 H. R. Byon, J. Suntivich and Y. Shao-Horn, *Chem. Mater.*, 2011, **23**, 3421–3428.
248 K. Kamiya, K. Hashimoto and S. Nakanishi, *Chem. Commun.*, 2012, **48**, 10213–10215.
249 X. Q. Xie, J. L. Long, J. Xu, L. M. Chen, Y. Wang, Z. Z. Zhang and X. X. Wang, *RSC Adv.*, 2012, **2**, 12438–12446.
250 R. T. Lv, T. X. Cui, M. S. Jun, Q. Zhang, A. Y. Cao, D. S. Su, Z. J. Zhang, S. H. Yoon, J. Miyawaki, I. Mochida and F. Y. Kang, *Adv. Funct. Mater.*, 2011, **21**, 999–1006.
251 H. Z. Dong, J. C. Bai, Q. Q. Zhu, J. H. Yu, L. Y. Yu and L. F. Dong, *J. Renewable Sustainable Energy*, 2013, **5**, 021405.
252 J. D. Roy-Mayhew, D. J. Bozym, C. Punckt and I. A. Aksay, *ACS Nano*, 2010, **4**, 6203–6211.
253 X. B. Xu, D. K. Huang, K. Cao, M. K. Wang, S. M. Zakeeruddin and M. Gratzel, *Sci. Rep.*, 2013, **3**, 1489.
254 Y. H. Xue, J. Liu, H. Chen, R. G. Wang, D. Q. Li, J. Qu and L. M. Dai, *Angew. Chem., Int. Ed.*, 2012, **51**, 12124–12127.
255 X. Y. Zhang, S. P. Pang, X. Chen, K. J. Zhang, Z. H. Liu, X. H. Zhou and G. L. Cui, *RSC Adv.*, 2013, **3**, 9005–9010.
256 M. J. Ju, J. C. Kim, H.-J. Choi, I. T. Choi, S. G. Kim, K. Lim, J. Ko, J.-J. Lee, I.-Y. Jeon, J.-B. Baek and H. K. Kim, *ACS Nano*, 2013, **7**, 5243–5250.
257 S. Das, P. Sudhagar, V. Verma, D. Song, E. Ito, S. Y. Lee, Y. S. Kang and W. Choi, *Adv. Funct. Mater.*, 2011, **21**, 3729–3736.
258 X. M. Li, D. Xie, H. Park, M. Zhu, T. H. Zeng, K. L. Wang, J. Q. Wei, D. H. Wu, J. Kong and H. W. Zhu, *Nanoscale*, 2013, **5**, 1945–1948.
259 G. H. Jun, S. H. Jin, B. Lee, B. H. Kim, W.-S. Chae, S. H. Hong and S. Jeon, *Energy Environ. Sci.*, 2013, **6**, 3000–3006.
260 Y. Y. Shao, S. Zhang, M. H. Engelhard, G. S. Li, G. C. Shao, Y. Wang, J. Liu, I. A. Aksay and Y. H. Lin, *J. Mater. Chem.*, 2010, **20**, 7491–7496.
261 G. H. Yang, Y. H. Zhou, J. J. Wu, J. T. Cao, L. L. Li, H. Y. Liu and J. J. Zhu, *RSC Adv.*, 2013, **3**, 22597–22604.
262 Y. Wang, Y. Y. Shao, D. W. Matson, J. H. Li and Y. H. Lin, *ACS Nano*, 2010, **4**, 1790–1798.
263 Z. H. Sheng, X. Q. Zheng, J. Y. Xu, W. J. Bao, F. B. Wang and X. H. Xia, *Biosens. Bioelectron.*, 2012, **34**, 125–131.
264 S. M. Li, S. Y. Yang, Y. S. Wang, C. H. Lien, H. W. Tien, S. T. Hsiao, W. H. Liao, H. P. Tsai, C. L. Chang, C. C. M. Ma and C. C. Hu, *Carbon*, 2013, **59**, 418–429.
265 H. X. Fan, Y. Li, D. Wu, H. M. Ma, K. X. Mao, D. W. Fan, B. Du, H. Li and Q. Wei, *Anal. Chim. Acta*, 2012, **711**, 24–28.
266 P. P. Guo, F. Xiao, Q. Liu, H. F. Liu, Y. L. Guo, J. R. Gong, S. Wang and Y. Q. Liu, *Sci. Rep.*, 2013, **3**, 3499.
267 Y. X. Huang, X. C. Dong, Y. X. Liu, L. J. Li and P. Chen, *J. Mater. Chem.*, 2011, **21**, 12358–12362.
268 Y. Q. Wen, F. B. Y. Li, X. C. Dong, J. Zhang, Q. H. Xiong and P. Chen, *Adv. Healthcare Mater.*, 2013, **2**, 271–274.
269 Y. H. Zhang, Y. B. Chen, K. G. Zhou, C. H. Liu, J. Zeng, H. L. Zhang and Y. Peng, *Nanotechnology*, 2009, **20**, 185504.
270 Y. H. Zhang, L. F. Han, Y. H. Xiao, D. Z. Jia, Z. H. Guo and F. Li, *Comput. Mater. Sci.*, 2013, **69**, 222–228.
271 J. Y. Dai and J. M. Yuan, *Phys. Rev. B: Condens. Matter Mater. Phys.*, 2010, **81**, 165414.
272 F. Niu, J. M. Liu, L. M. Tao, W. Wang and W. G. Song, *J. Mater. Chem. A*, 2013, **1**, 6130–6133.
273 H. Xu, L. M. Xie, H. L. Zhang and J. Zhang, *ACS Nano*, 2011, **5**, 5338–5344.
274 X. K. Kong and Q. W. Chen, *J. Mater. Chem.*, 2012, **22**, 15336–15341.
275 R. Lv, Q. Li, A. R. Botello-Mendez, T. Hayashi, B. Wang, A. Berkdemir, Q. Z. Hao, A. L. Elias, R. Cruz-Silva, H. R. Gutierrez, Y. A. Kim, H. Muramatsu, J. Zhu, M. Endo, H. Terrones, J. C. Charlier, M. H. Pan and M. Terrones, *Sci. Rep.*, 2012, **2**.
276 V. Tozzini and V. Pellegrini, *Phys. Chem. Chem. Phys.*, 2013, **15**, 80–89.

277 V. B. Parambhath, R. Nagar and S. Ramaprabhu, *Langmuir*, 2012, **28**, 7826–7833.
278 S. Lee, M. Lee, H. Choi, D. S. Yoo and Y. C. Chung, *Int. J. Hydrogen Energy*, 2013, **38**, 4611–4617.
279 S. Lee, M. Lee and Y. C. Chung, *Phys. Chem. Chem. Phys.*, 2013, **15**, 3243–3248.
280 Y. G. Zhou, X. T. Zu, F. Gao, J. L. Nie and H. Y. Xiao, *J. Appl. Phys.*, 2009, **105**, 014309.
281 E. Beheshti, A. Nojeh and P. Servati, *Carbon*, 2011, **49**, 1561–1567.
282 K. C. Kemp, V. Chandra, M. Saleh and K. S. Kim, *Nanotechnology*, 2013, **24**, 235703.
283 W. L. Wei, C. Xu, L. Wu, J. S. Wang, J. S. Ren and X. G. Qu, *Sci. Rep.*, 2014, **4**, 3564.
284 Q. Liu, B. D. Guo, Z. Y. Rao, B. H. Zhang and J. R. Gong, *Nano Lett.*, 2013, **13**, 2436–2441.
285 D. Sun, R. Ban, P. H. Zhang, G. H. Wu, J. R. Zhang and J. J. Zhu, *Carbon*, 2013, **64**, 424–434.
286 A. D. Zhao, C. Q. Zhao, M. Li, J. S. Ren and X. G. Qu, *Anal. Chim. Acta*, 2014, **809**, 128–133.

 